

Data-driven simulations elucidate how lymphocyte motility behaviors drive cell-cell interactions within germinal centers.

Nikita Sivakumar^{1,2,3}, Chanhong Min^{1,2,3}, Kibaek Choe⁴, Wendy Béguelin⁵, Jude M. Phillip^{2,3,6,7,8,*}, Feilim Mac Gabhann^{1,2,3,*}

¹Institute of Computational Medicine, Johns Hopkins University, Baltimore, MD, USA

²Institute of NanoBiotechnology, Johns Hopkins University, Baltimore, MD, USA

³Department of Biomedical Engineering, Johns Hopkins University, Baltimore, MD, USA

⁴School of Applied and Engineering Physics, Cornell University, Ithaca, NY, USA

⁵Department of Medicine, Division of Hematology and Medical Oncology, Weill Cornell Medicine, New York, NY, USA

⁶Department of Chemical and Biomolecular Engineering, Johns Hopkins University, Baltimore, MD, USA

⁷Department of Oncology, Sidney Kimmel Comprehensive Cancer Center, Johns Hopkins School of Medicine, Baltimore, MD, USA

⁸Translational Tissue Engineering Center (TTEC), Johns Hopkins University, Baltimore, MD, USA

*Co-Corresponding Authors

ABSTRACT

Lymphocytes rely on cell motility to surveil immune microenvironments and engage in contact-mediated interactions with other cells as part of the adaptive immune response. Within the germinal center (GC) light zone, germinal center B-cells (GCBs) and T-follicular helper cells (Tfh) engage in cell-cell interactions that enable antibody affinity maturation. The number and duration of GCB-Tfh interactions correlate with the success of the germinal center in effectively generating antibodies that can bind and neutralize antigens. Prior studies have shown that GCBs and Tfh exploit distinct motility patterns to surveil the GC light zone and engage in these cell-cell interactions. However, the quantitative relationship between lymphocyte motility parameters (such as speed and tortuosity) and GCB-Tfh interactions has not been systematically explored. Here, we analyzed single-cell trajectories of GCBs and Tfh from two-photon intravital microscopy videos of GCs within mouse popliteal lymph nodes. We found that these cells exhibit seven distinct motility behaviors, each with characteristic speeds and tortuosities. GCBs tended to move in slow and tortuous paths, while Tfh adopted faster and more directed trajectories. We then developed a three-dimensional agent-based model (ABM) to simulate these experimentally-observed GCB and Tfh motility behaviors and predict their impact on GCB-Tfh interactions. Using the ABM, we found that the baseline motility behaviors of GCBs and Tfh allow GCBs to maximize interactions with distinct Tfh in a confined space.

INTRODUCTION

Lymphocytes are intrinsically “motile”, and the speed and pattern of their movement drive cell-cell interactions that enable key elements of the adaptive immune response (1–5). Lymphocytes exploit distinct “motility behaviors” characterized by unique speeds and tortuosities to surveil their local microenvironment. Disruption of baseline lymphocyte motility behaviors can disrupt physiological cell-cell interactions and lead to disease. Systematically understanding how distinct motility behaviors drive dynamic cell-cell interactions can yield critical insights into how motility properties could be tuned to modulate cell-cell interactions that carry out the immune response. Here, we present a computational pipeline that leverages intravital imaging to learn *in vivo* lymphocyte motility behaviors and mechanistically simulate these behaviors to predict their impact on multi-cell interactions.

To develop this pipeline, we focused on B and T-cell motility during the peak of the germinal center (GC) reaction. The GC reaction involves interactions between germinal center B-cells (GCBs) and T-follicular helper cells (Tfh) that enable the selection and mutation of the hypervariable region of immunoglobulin genes of B-cell clones, in order to produce high-affinity antibodies against antigen (6–11). GCs are polarized into a dark zone and light zone. Within the dark zone, GCBs undergo rapid proliferation and somatic hypermutation, generating distinct antibody clones. Dark zone GCBs then migrate to the light zone, which is organized by a dense network of follicular dendritic cells (FDCs). Within the GC light zone, GCBs internalize antigen from FDCs and present them to Tfh. The affinity of this GCB-Tfh interaction determines the fate of that GCB, such that high affinity interactions provide cues for that GCB to mature into an effector cell or recirculate to the dark zone for further rounds of mutation. Therefore, GCB-Tfh interactions are essential for antibody affinity maturation. GCBs and Tfh rely on cell motility to navigate the GC light zone and engage in GCB-Tfh interactions (3,12–16). Dysregulated lymphocyte motility leads to diminished antibody response (17,18). However, the relationship between lymphocyte motility and GCB-Tfh interactions within the GC light zone is not well understood. Here, we leverage *in vivo* imaging of mouse GCs along with computational approaches to systematically quantify this relationship.

Two-photon intravital time-lapse microscopy enables live-cell imaging of lymphocyte motility and interactions within *in vivo* germinal centers (13,19–21). This imaging approach captures high-resolution movies of single-cell GCB and Tfh trajectories by selectively labelling a small subset of GCBs and Tfh within the mouse GC so that these cells can be differentiated from the dense GC microenvironment. As a result of this sparse labeling, the approach yields high-quality data but captures trajectories of only a subset of the cells and only a subset of all the GCB-Tfh cell-cell interactions taking place, because most cells are unlabeled. A limitation of this sparse labelling is that labelled proportions of lymphocytes within the imaged volume may not closely approximate the relative ratios of these cell types in the actual system (i.e. a different % of the GCB cells may be labeled than the Tfh cells). Therefore, while we can gather insights about GCB-Tfh interactions from intravital imaging, these measurements may be biased. Here, we have developed a computational pipeline that builds upon intravital data to recreate the movements and interactions of cells at full GC density. This pipeline can calculate the ‘unseen’ interactions between unlabeled cells and provide additional insights on how lymphocyte motility drive GCB-Tfh interactions.

Our computational approach, **PRISMM** (**P**ipeline for **R**ecapitulating Cell-Cell **I**nteractions Using **S**patial **M**otility **M**odeling) uses a combination of unsupervised machine learning and mechanistic computational modelling. Previously, we developed a machine-learning framework—CaMI to identify motility behaviors across single-cell trajectories by integrating several motility features (1). Unlike bulk analysis approaches, CaMI allows us to assess the heterogeneity of movement patterns that a cell may exploit to carry out key biological functions. Here, we have expanded this unsupervised learning approach to characterize emergent motility behaviors across 3D single-cell GCB and Tfh trajectories. We then developed and validated an agent-based model (ABM) to simulate these learned cell motility behaviors within multi-cell environments and predict how these motility behaviors influenced the likelihood of GCB-Tfh interaction. Our ABM simulates how individual cells moving according to distinct motility properties (i.e. speed, tortuosity) can emergently co-localize and interact with each other. PRISMM uses a parallel approach that directly compares motility features quantified from cell trajectories obtained via time-lapse *in vivo* imaging with motility features quantified from simulated trajectories within *in silico* agent-based models. We ran ABMs seeded with the full density of GCBs and Tfhs expected within the GC environment to predict the full extent of GCB-Tfh interactions within GCs. Moreover, after validating these predictions, we systematically explored how observed GCB and Tfh motility behaviors influenced GCB-Tfh interactions. In this way, our computational pipeline leverages insights from intravital microscopy data to predict underlying mechanisms of GCB-Tfh interactions (**Figure 1**).

RESULTS

Intravital imaging enables single-cell tracking of GCBs and Tfhs within the germinal center light zone.

To analyze the motility behaviors of germinal center lymphocytes, we used imaging data from mixed bone marrow chimeric mice with fluorescently-labelled Tfhs and GCBs. We performed two-photon (2P) intravital microscopy on mouse popliteal lymph nodes at the peak of the germinal center reaction (9-11 days post-immunization with NP-OVA) to acquire single-cell motility data and cell-cell interaction data between Tfhs and GCBs. We captured three-dimensional (3D) time-lapse images ($231\text{ }\mu\text{m} \times 231\text{ }\mu\text{m} \times 90\text{ }\mu\text{m}$ volume) at 30-second intervals for a total of 89.5 minutes (180 frames). We then used IMARIS to segment and track individual cells within each time-lapse movie. Collectively, we obtained 9,720 single-cell trajectories (4,194 Tfhs; 5,526 GCBs), each trajectory lasting 9.5 minutes.

Initial cell behavior analysis identifies outlier lymphocyte trajectories.

To quantify behavioral phenotypes across the experimentally-obtained lymphocyte trajectories, we extracted 36 motility features from each trajectory. These features described the overall displacement and angular displacement properties of each trajectory (**Figure 2, Table 1**). We then performed feature selection and unsupervised clustering to identify clusters of cell trajectories with emergently similar motility feature values and visualized characteristics of these clusters (**Supplemental Figure 1**, described in detail in **Supplemental Text S1**). We found that one cluster predominantly contained trajectories with high displacement kurtosis and skewness values. Displacement kurtosis and skewness measure the degree to which the distribution of displacements deviates from a normal distribution. Within trajectories that only comprise 20 frames, we would not expect significant deviations from a normal distribution. The cluster with high displacement kurtosis and skewness values contained trajectories with outlier displacements that could be representative of mis-segmented trajectories. We developed a method to eliminate such outlier trajectories (**Supplementary Figure 2**, described in detail in **Supplemental Text S1**). Following the elimination of the outliers, the curated dataset consisted of 6,912 trajectories. Among the remaining trajectories, a small percentage of trajectories still showed slightly higher displacement kurtosis values than expected. Using Monte-Carlo simulations, we found that these trajectories had high kurtosis because of biases introduced by low sampling frequency (**Supplementary Figure 3**, described in detail in **Supplemental Text S1**). We thus omitted kurtosis features from further analysis of the data, reducing the number of motility features by 5 to 31.

Tfhs and GCBs exhibit distinct motility phenotypes.

After data quality control and the elimination of outlier trajectories, we performed feature selection and unsupervised clustering on the cleaned data to understand GCB and Tfh cell motility behaviors. The cleaned dataset contained 6,912 trajectories and 31 motility features. Principal component analysis (PCA) indicated that 3 principal components (PCs) explained 75% of the data. A factor analysis on these 3 PCs yielded a communality score for each motility feature that ranks the degree of variance each feature contributes to these 3PCs. 26 features had a

communality score greater than 0.5 (**Supplementary Figure 4A**). The major feature groups within the reduced features space included average speed, MSD features in the primary, secondary, and tertiary axes, net distance, and progressivity (**Supplementary Figure 4B**).

For ease of visualization, we constructed a 2D UMAP embedding of the 6,912 cell trajectories based on the 26 motility features. To determine whether Tfhs and GCBs had distinct motility behaviors, we colored each trajectory in the UMAP by cell type. We found that Tfhs and GCBs occupied distinct subspaces within the 2D UMAP (**Figure 3A**). Displacement features appeared to horizontally differentiate trajectories in the UMAP space (**Figure 3B**), while tortuosity features appeared to vertically differentiate trajectories in the UMAP space (**Figure 3C**). Tfhs and GCBs were horizontally separated in the UMAP space (**Figure 3A**). Accordingly, Tfhs had significantly higher average speeds and MSDs at one-minute intervals than GCBs (**Figure 3B**). Tfhs and GCBs were distributed over a wide vertical range of the UMAP, suggesting that both cell types had a wide range of tortuosity characteristics. However, Tfhs occupied a smaller vertical space than the GCBs and accordingly had significantly lower progressivity and significantly higher net distance than the GCBs (**Figure 3C**). This trend suggests that Tfhs bulk movement is faster and more tortuous than GCB bulk movement.

To identify distinct classes of motility behaviors, we first performed hierarchical clustering of the motility feature space. Hierarchical clustering of the data (**Figure 3D**) yielded two motility classes that occupied horizontally distinct hemispheres of the motility space (C1, C2; **Figure 3E**). C1 had a significantly higher average speed than C2 (**Figure 3F**). While both behavioral classes comprised a larger range of progressivity values, C2 had a slightly higher progressivity than C1 and comprised more directed trajectories than C1 (**Figure 3F**). Consistent with the finding that Tfhs had higher mean displacements than GCBs, C1 contained a higher proportion of Tfhs (80%) and C2 contained a lower proportion of Tfhs (17%) (**Figure 3G**). This result indicates that Tfhs exhibit a bias towards high-speed motility states.

To classify the trajectories into discrete motility behaviors, we performed unsupervised k -means clustering (1). This method provided an alternate subdivision of trajectories into seven discrete motility behaviors (B1-B7, **Figure 3H-I**). We used inertia and concordance analyses to select k as the number of clusters that minimize within-cluster variance without overfitting (see *Methods*, **Supplementary figure 4C-D**). Each motility behavior had characteristic displacement and tortuosity values (**Figure 3H-J**, **Supplementary Figure 4E**). These clusters exhibited distinct “high” or “low” states of progressivity, whereas the previous two-cluster analysis did not. Tfhs had a higher occurrence across B1-B4 (faster moving clusters), while GCBs had a higher occurrence across B5-B7 (slower moving clusters) (**Figure 3K**).

Agent-based simulation recapitulates experimentally-observed single-cell behaviors.

After discovering distinct motility behaviors across GCBs and Tfhs within GCs, we wanted to simulate these trajectories to derive deeper insights into how single-cell motility properties map to multi-cell interaction dynamics. We developed a 3D, on-lattice agent-based simulation in which cell agents execute movement rules at each timestep. Because displacement and tortuosity features were key differentiators of the experimental trajectories, we designed the cell movement

rule to have two parameters that can directly modulate these motility features. When a cell agent moves, it evaluates a move probability (*MP*)—the likelihood of moving forward, and a turn probability (*TP*)—the likelihood that the cell will turn on that timestep. Each cell agent has its own values of *MP* and *TP*. Because this movement rule is probabilistic, a (*MP*, *TP*) parameter combination can give rise to one of a large population of possible trajectories; however, the motility features of this trajectory will be at least partially dependent on *MP* and *TP*. In order to use the agent-based simulation to recapitulate experimentally-observed trajectories we explored how simulated parameters affect distinct motility features, calibrated the spatiotemporal resolution of the simulation, and then optimized specific (*MP*, *TP*) parameter distributions to recapitulate each experimentally observed motility behavior (**Figure 4A**).

To quantify how *MP* and *TP* affect motility features of simulated trajectories, we ran single-cell (SC) simulations for distinct *MP* and *TP* values. SC simulations model individual cell agents evaluating *MP* and *TP* on each timestep to move with no external barriers to movement (see **Methods**). We sampled *MP* uniformly from 0.05 to 0.95 (19 unique *MP* values), and we sampled *TP* from 0 to 1 (16 unique *TP* values). In these initial single-cell simulations, we used a voxel size of 4 μm and a temporal resolution of 30 seconds per timestep (i.e. the same temporal resolution as the experimental data). The average speed (**Figure 4B**) and MSD at 1-minute intervals (**Figure 4C**) increased linearly with respect to *MP*, such that higher *MP* values give rise to higher simulated displacement. The progressivity of simulated trajectories tended to increase with respect to *TP* (**Figure 4D**). The net distance depended on both *MP* and *TP*; the net distance of the trajectory increased as *MP* increased, while the net distance decreased as *TP* increased (**Figure 4E**).

Global parameter search determines optimal spatiotemporal resolution to recapitulate experimentally observed behaviors.

In addition to *MP* and *TP*, the spatial and temporal resolution of the simulation regulates the motility properties of cell agents within the simulation. The on-lattice simulation assumes that cells can only move between adjacent lattice spaces. Therefore, the spatial resolution indicates the size of each voxel in the simulation lattice environment and controls how far a cell can move on a discrete timestep of the simulation. The temporal resolution indicates how long each timestep of the simulation represents and thus controls the overall range of movement (i.e. higher temporal resolutions necessitate larger run times to match experimental trajectory duration, resulting in a greater possible number of moves). To ensure accurate comparison with experimental trajectories, we down-sampled simulated trajectories to the framerate of the experimental trajectories before motility feature extraction.

We next sought to quantify how the spatiotemporal resolution affects simulated motility features within SC simulations. First, we ran SC simulations for a fixed *MP* = 0.95 and *TP* = 0.0 for several combinations of spatial resolutions (4 μm , 2 μm , 1 μm per voxel dimension) and temporal resolutions (30, 15, 7.5, and 5 seconds per timestep). For each spatiotemporal resolution, we quantified the fold change in values for displacement and tortuosity features with respect to trajectories generated using a spatial resolution of 4 μm per voxel dimension and a temporal resolution of 30 seconds per timestep (**Supplementary Figure 5A**). When cells were moving unidirectionally, the values of displacement features increased proportionally with temporal

resolution— i.e., doubling the temporal resolution doubled the average speed or quadrupled the mean squared displacement. This phenomenon arises because increasing the temporal resolution by a factor of 2 (30 to 15 seconds per time step) doubles the required run time to recapitulate a 10-minute experimental trajectory and, accordingly, doubles the possible number of moves a cell agent could make. Therefore, doubling the temporal resolution can double the maximum simulated average speed. Conversely, the values of displacement features decreased proportionally with spatial resolution— i.e., increasing the spatial resolution by a factor of 2 (e.g. from 4 μ m to 2 μ m per voxel dimension), halved the distance cell agents travel per timestep and accordingly reduced the average speed by a factor of 2 and the mean squared displacement at 1-minute intervals by a factor of 4.

We next repeated this analysis for a fixed $MP = 0.95$ and $TP = 0.9$ to quantify how spatiotemporal resolution affects motility features when the cell agent is also turning (**Supplementary Figure 5B**). We found that the magnitude changes in displacement features in response to increasing temporal resolution were less than those compared to when the cells are moving unidirectionally (**Supplementary Figure 5A**). This result likely arises due to down-sampling of simulated trajectories that were generated at higher temporal resolutions than the experiment. Due to this down-sampling, at temporal resolutions greater than the experimental framerate, high TP values could lead to turning behaviors that reduce the quantified displacement of the down-sampled trajectory, but not the trajectory at the simulation framerate. The effect of spatial resolution did not change in response to increasing TP . Additionally, spatiotemporal resolution appeared to have minimal effect on progressivity values.

We next sought to calibrate the spatial and temporal resolution of the simulation, such that the simulation could generate trajectories that capture the range of experimentally-observed motility feature distributions. For each spatiotemporal resolution pair, we generated a “simulated trajectory space” by aggregating trajectories from simulations run with different MP and TP values between 0 and 1. By globally sampling MP and TP for each spatiotemporal resolution pair, we can assess the entire possible universe of trajectories that each spatiotemporal resolution can generate (**Supplementary Figure 5C-D**). As our prior analyses suggested (**Supplementary Figure 5A**), increasing the spatial resolution of the simulation (i.e. decreasing the size of each voxel dimension) decreased the range of movement of the cell agents. Simultaneously, increasing the temporal resolution (i.e. decreasing the size of the simulation timestep) expanded the range of movement of the cell agent (**Supplementary Figure 5C**). Interestingly, at temporal resolutions higher than the frame rate of experimentally measured trajectories, the average speed of simulated trajectories became dependent on both MP and TP (**Supplementary Figure 5C**). This result arises because when down-sampling simulated trajectories at temporal resolutions greater than the experimental framerate, high TP values could lead to turning behaviors that reduce the overall displacement of the down-sampled trajectory. Therefore, at high temporal resolutions, the average speed at a given MP decreases as TP increases. Tortuosity features, such as progressivity, did not appear to experience changes in MP or TP dependence with respect to spatiotemporal resolution (**Supplementary Figure 5D**).

To calibrate model spatiotemporal resolution, we compared the range of each motility feature for the aggregated simulated trajectories from a given spatiotemporal resolution to that of the experimental trajectories. We were not at this point attempting to match the experimental

distributions precisely but rather ensuring that the model had the ability to capture it. We computed several metrics to assess the extent to which the simulation can cover experimentally-observed ranges. The number of covered features indicates out of 26, the number of features for which the simulation captures the full experimentally-observed range; ideally, this number should be as close to 26 as possible (**Figure 4F**). The mean feature coverage indicates, on average, the fraction of the experimentally-observed range that the simulation set captures for each motility feature; ideally, we want this metric to be as close to 1 as possible (**Figure 4G**). Finally, the mean feature overshoot indicates the average log 10 ratio of the simulation range to the experimental range for each motility feature; ideally, we want this number to be greater than 0, but not significantly greater than 0 to prevent significant overshoot of experimental motility feature distributions (**Figure 4H**). We find that the values for the metrics described above were different for each spatiotemporal resolution, but consistent between the single-cell and multi-cell simulations. The spatiotemporal resolution that maximized mean feature coverage and number of covered features, while minimizing mean feature overshoot, was a spatiotemporal resolution of 2 μm per voxel dimension and a timestep size of 7.5 seconds (77 timesteps) in both single-cell and multi-cell simulations.

Motility parameters do not approximate the same motility behaviors in single- and multi-cell contexts.

After calibrating the spatiotemporal resolution for the simulation, we sought to find distributions of values for *MP* and *TP* that, when used as input to the simulations, yield a population of simulated trajectories similar to those that comprise each experimental motility behavior.

We first used the single-cell (SC) simulation to simulate several trajectories per (*MP*, *TP*) combination with *MP* and *TP* ranging from 0 to 1. We ran our simulations at the previously determined optimal spatial resolution of 2 μm per voxel dimension and temporal resolution of 7.5 seconds per time step. To assess which (*MP*, *TP*) values give rise to trajectories most similar to each experimental motility behavior, we computed the aggregated minimum distances between the simulated trajectories generated by each (*MP*, *TP*) combination and the experimental trajectories that compose each experimental motility behavior (**Figure 4I**). When visualizing the (*MP*, *TP*) combinations for which the aggregated minimum distance was in the bottom tenth percentile, we found each experimental motility behavior corresponded to a unique subspace of *MP* and *TP* values. We next assessed whether the (*MP*, *TP*) combination with minimum aggregated distance to each experimental motility behavior generated motility feature distributions that are similar to those of the experiment (**Supplementary Figure 6A**). We quantified the Cohen's D between simulated motility feature distributions and experimental feature distributions for each motility behavior. The Cohen's D metric measures the relative standard deviation difference between two distributions and a value less than or equal to 0.5 indicates a low effect size. We found that the closest (*MP*, *TP*) combination in the SC simulation had high dissimilarity with experimental motility features (54% of motility features had a Cohen's D > 0.5). Motility behaviors B5-B7 had high dissimilarity across several displacement features, suggesting that the closest (*MP*, *TP*) combination did not effectively recapitulate low-speed trajectories. Based on this observation, we aimed to combine several (*MP*, *TP*) values to accurately recapitulate experimental motility feature distributions for each motility behavior.

We employed an evolutionary algorithm to find the optimal proportions by which to sample distinct (MP , TP) combinations, such that the mixed distribution of (MP , TP) gives rise to simulated trajectories emergently similar to those in each experimental motility behavior (**Figure 4J**). We then compared simulated motility feature distributions generated from this mixed parameter distribution with the experimental data (**Supplementary Figure 6B**). Similarity was significantly improved, with ~13% of motility features having a Cohen's $D > 0.5$. These features primarily comprised progressivity values in the primary and secondary axis of movement. While these initial parameterizations were run in SC simulations, we ultimately needed to run multi-cell (MC) simulations with these parameters to predict how cell motility drives cell-cell interaction. These multi-cell simulations would consider additional rules to prevent cell-cell overlap when moving (see **Methods**). An important consideration is whether these additional rules to avoid cell-cell overlap cause a given (MP , TP) value to give rise to different motility feature values between the SC and MC simulations. To assess this aspect, we next ran multi-cell simulations at 50% cellular density that sample the mixed parameter distributions derived from SC simulations (**Supplementary Figure 6C**). We found that dissimilarity in these MC simulations increases (~26% of motility features have a Cohen's $D > 0.5$). The MC simulation particularly underestimated high displacement values and high progressivity values, which primarily comprised the 26% of dissimilar features (**Figure 4K-L**). Trajectories in the MC simulation also didn't accurately recapitulate motility behaviors that were highly directed (**Figure 4M-N**). This result suggests that a given MP and TP value in SC simulations does not give rise to the same motility feature values in MC simulations.

Cell motility behaviors change in multi-cell environments.

Multi-cell simulations contain several additional rules to avoid cell agent overlap (**Figure 5A**). To assess how multi-cell environments affect motility features for MP and TP parameter values, we performed multi-cell (MC) simulations that sampled the same MP and TP parameter space as previously considered SC simulations for a fixed spatial resolution of 4 μm per voxel dimension and temporal resolution of 30 seconds per simulation timestep (**Figure 5B-E**).

As in SC simulations, displacement directly increased with respect to MP in MC simulations at the same temporal resolution as the experimental data. However, for a given value of MP , trajectories from MC simulations appeared to have lower displacement than those from single-cell simulations (**Figure 5B-C**). This phenomenon likely arises because in MC simulations, cell agents may fail to move on some time steps due to obstructions preventing movement. Therefore, for a given MP value, cell agents in multi-cell simulations effectively make fewer moves than those within single-cell simulations. The degree to which displacement in the MC simulation is less than the SC simulation was also TP -dependent. For a given (MP , TP) combination, the log fold-change between MC and SC values for displacement decreased uniformly as TP decreased (**Figure 5B-C**). This trend likely arises because a cell agent in the MC simulation is more likely to fail to move when the TP is lower, resulting in decisions to move persistently. When a cell agent that chooses to move persistently in the MC simulation faces an obstruction in the lattice space ahead, that agent will move to a lattice space that is a shared neighbor of the current lattice space and the lattice space ahead (**Figure 5A**). The number of choices to move to a non-obstructed space is

fewer than if the cell were to move non-persistently and could turn to any of the surrounding lattice spaces.

As in SC simulations, progressivity values of simulated trajectories in MC simulations decreased as *TP* increased (**Figure 5D**). MC simulations appeared to have an overall lower range of progressivity values (0.23-1.0) than SC simulations (0.22-0.70). This trend also likely arises due to the cell agent's decision to avoid obstructions during persistent movement (i.e., if a cell agent that chooses to move persistently in the multi-cell simulation faces an obstruction in the lattice space ahead, that agent will move to a lattice space that is a shared neighbor of the current lattice space and the lattice space ahead). While this decision minimizes turn angles, this action still results in non-directed movement, leading to a decreased progressivity value. These decisions to avoid obstructions during persistent movement are likely to account for lower progressivity values for lower *TP* values in the multi-cell simulation compared to the single-cell simulation. In both SC and MC simulations, the net distance of simulated trajectories increased for higher *MP* values and decreased for higher *TP* values (**Figure 5E**). The maximum net distance in the MC simulation was 48.5 μm , while the maximum net distance in the SC simulation was 102.8 μm . The lower net distance achieved by the MC simulation is consistent with how decisions to avoid obstacles lead to lower movement for a given *MP* value, and even lower movement at lower *TP* values.

These results indicate that cells moving within multi-cell environments have fundamentally different motility behaviors due to the necessity to avoid surrounding obstructions. These observations indicate that parameterization for *MP* and *TP* should be conducted within MC simulations that reflect how obstructions distort cell motility instead of SC simulations. Accordingly, we repeated the mixture modeling approach for parameterization in multi-cell simulations to derive (*MP*, *TP*) parameter distributions for each of the seven experimentally-observed motility behaviors. As in SC simulations, we found that the closest (*MP*, *TP*) combination did not yield the best overall fit across all motility features (**Figure 5F**, **Supplementary Figure 6D**). However, the optimized mixed distribution of *MP* and *TP* (**Figure 5G**) yielded significantly improved fits to the experimental data that were reproducible when running new MC simulations that re-sampled these parameter distributions (**Figure 5H**, **Supplementary Figure 6E-F**). 12% of motility features across all motility behaviors had a Cohen's *D* > 0.5 for the trajectories that sampled MC mixed-parameter distributions (down from 26% when using SC parameter distributions). The dissimilar motility features included net distance and progressivity in the primary and secondary axes.

We compared the top-down parameterization approach described above with a bottom-up, *k*-nearest neighbors approach (**Supplemental Text S2**). This alternative approach computes the nearest simulated neighbor to each experimental trajectory and extracts the distribution of *MP* and *TP* that gave rise to the simulated neighbors as the (*MP*, *TP*) distribution for each motility behavior (**Supplementary Figure S7**). We found that this approach was not robust because the (*MP*, *TP*) combination that gave rise to a single trajectory that appeared to be similar to an experimental trajectory may not robustly reproduce this trajectory in future simulations. The chosen top-down approach is more robust because this approach accounts for the intrinsic variability across trajectories generated by a single (*MP*, *TP*) combination. The chosen approach accounts for this variability by assessing the overall similarity of a population of stochastically-generated trajectories from a given (*MP*, *TP*) combination with the set of experimentally-observed trajectories within each motility behavior, instead of comparing individual pairs of trajectories.

Simulation predictions recapitulate variation in experimentally-observed multi-cell interactions.

Each of the 15 experimental movies in our intravital microscopy dataset has a slightly different proportion of tracked (cells labelled and segmented for 20 continuous frames) and segmented GCBs and Tfhs (cells labelled and segmented for 5 continuous frames) (**Figure 6A**). This resulted in distinct measurements of total GCB-Tfh interactions between experiments (**Figure 6B**) per movie. To validate the ability of our simulations to predict GCB-Tfh interactions, we seeded simulations that recapitulated the percentage volume of tracked and segmented cells in the simulation to that in each experimental movie. To compute these percentage volumes in each experiment, we first examined a spatial histogram of tracked (**Supplementary Figure 8A**) and segmented (**Supplementary Figure 8B**) cell locations across all videos to see whether cells were uniformly dispersed throughout the imaging volume. We found that the imaged cells appeared to only be dispersed across the middle 70% of the imaged z-volume. Therefore, we computed the density of tracked and segmented cells as a proportion of seven-ninths of the experimental imaging volume. In the validation simulations, we also included populations of unlabeled GCBs and Tfhs that matched the expected proportion of these cells in the germinal center. The inclusion of these unlabeled cells allows the multi-cell simulations to: 1) account for cell movement based on the abundance of neighboring cell obstructions and 2) predict the expected level of interactions between GCBs and Tfhs within the overall germinal center, which may not be captured due to sparse labeling within the experimental volume.

Because our computational model is stochastic, we next assessed how many repetitions of the model are necessary to achieve reproducible estimates of tracked GCB-Tfh interactions for each experiment. This analysis is particularly important for this set of simulations because the tracked percentage volume of cells is <1% in each experiment, and we are estimating interactions over a very low sample size of cells that is prone to more noise. Simultaneously, to maximize computational efficiency, we tested running simulations at smaller volumes than the experimental volume. At smaller simulated volumes, the noise across simulated repetitions is higher (**Supplementary Figure 8C**). Therefore, reaching a stable estimate in smaller simulated volumes requires more repetitions. Conversely, achieving a stable estimate at larger volumes requires fewer repetitions. Given this trade-off between simulation size and # of repetitions, we opted to run simulations at the experimental volume with fewer repetitions ($n = 50$). At the experimental volume, we are able to simulate the exact numbers of tracked and segmented cells within each experiment. Additionally, by maximizing the number of segmented and tracked cells, we can be more confident in effective sampling of motility parameter distributions.

In the validation simulations, we modelled each cell type as a proportional distribution of the seven motility behaviors according to the occurrences quantified in **Figure 3K**. We found that predictions for Tfh interactions per GCB were highly correlated with experimental measurements (**Figure 6C**). GCB interactions per Tfh had lower correlation with experimental measurements (**Figure 6D**). Simulation predictions were consistently less than experimental measurements (**Figure 6E**). We hypothesize that this trend emerges because our model includes no additional rules for antibody-antigen affinity between GCBs and Tfhs. In the actual germinal center, GCBs and Tfhs have persistent interactions determined by the antibody-antigen binding affinity that could increase the total measured GCB-Tfh interactions.

Specific GCB and Tfh motility behaviors maximize unique GCB-Tfh interactions.

After validating that simulations can recapitulate experimentally-observed GCB-Tfh interactions, we ran multi-cell simulations to systematically quantify how single-cell motility behaviors affect overall GCB-Tfh interactions. We performed multi-cell simulations at 50% cellular density in which we varied the motility behavior of GCBs from B1-B7 and Tfhs from B1-B7 (**Figure 7**). We ran these simulations within a confined space over 10 minutes, the duration of experimentally-observed trajectories (i.e. when cells leave the simulation world, new cells enter instead of the same cell wrapping around the simulation world). In addition to the total number of interactions, we quantified the number of unique interactions experienced by each cell, defined as the number of distinct interaction partners. We found that out of all motility behavior combinations, Tfhs moving according to motility behaviors B1-B4 and GCBs moving according to motility behaviors B4-B7 yielded the maximum unique Tfh interactions per GCB (**Figure 7A**). This result is interesting because this breakdown reflects the baseline motility behaviors of GCBs and Tfhs measured experimentally (**Figure 3K**). We also found that, when Tfhs move according to motility behaviors B5-B7, unique Tfh interactions per GCB are greater when GCBs move according to motility behaviors B2 and B4. This result suggests that when Tfhs (which comprise a smaller proportion of the simulated cells) are moving more slowly, GCBs moving according to faster and more tortuous motility behaviors enable slightly greater unique cell-cell interactions. Conversely, unique GCB interactions per Tfh are maximized when Tfhs move according to motility behaviors B4-B7 and GCBs move according to motility behaviors B1-B4 (**Figure 7B**). The total Tfh interactions per GCB, on the other hand, increase uniformly as GCB speed decreases (**Figure 7C**). Total Tfh interactions do not consider the unique identity of cells and simply count the number of time-steps a GCB neighbors a Tfh; therefore, when a cell does not move, it maximizes its ability to have cells surrounding it at all times. Similarly, total GCB interactions per Tfh increase as Tfh speed increases (**Figure 7D**).

We next ran this parameter space exploration in an unconfined volume (i.e. cells wrap around the simulation volume and maintain the same identity. Within an unconfined volume, the trend shift towards both GCBs and Tfhs moving according to fast motility behaviors (B1-B4) yielded the highest number of unique GCB-Tfh interactions (**Figure 7E-F**). This trend arises because in an unconfined space, both cells moving as fast as possible allow the cells to surveil the maximum amount of space and engage in cell-cell interactions. Moreover, the total GCB-Tfh interactions do not change as a function of motility behavior (**Figure 7G-H**) because cells are always able to persistently interact with neighboring cells, and there's no turnover in the cells that can be encountered.

Taken together, these simulations suggest that within a confined space, GCBs moving slowly allow them to stay in place and maximize their ability to encounter fast-moving Tfhs (**Figure 7I**).

DISCUSSION

In this study, we present **PRISMM**, a data-driven and mechanistic approach to quantify heterogeneous lymphocyte motility behaviors and predict how these motility behaviors contribute to the likelihood of cell-cell interaction. Our pipeline uses unsupervised clustering to identify single-cell motility behaviors from *in vivo* lymphocyte trajectories. PRISMM then uses three-dimensional agent-based simulations to mechanistically predict how these motility behaviors influence the likelihood of GCB-Tfh interactions. Using PRISMM, we identified seven distinct lymphocyte motility behaviors with characteristic speeds and tortuosities. We found that Tfhs tend to occupy motility behaviors characterized by high cell speeds, while GCBs were abundant in low-speed motility behaviors.

When attempting to simulate these experimentally-observed motility behaviors, we initially used single-cell simulations that are faster to execute because they do not contain rules to avoid obstructions. However, we found that motility in single-cell versus multi-cell contexts is fundamentally different, because volumetric exclusion rules lead to altered motility within multi-cell environments. Cell motility within multi-cell environments is intrinsically altered by the avoidance of surrounding obstructions. This behavior suggests that cell motility measured in dense environments may be distinct from that measured in less dense environments.

After validating simulation predictions, we used our simulation to systematically predict how GCBs and Tfhs moving according to each of the seven observed motility behaviors influences cell-cell interaction. We found that within a confined motility space, the number of unique Tfh interactions per GCB was predicted to be highest when Tfhs moved according to motility behaviors B1-B4 and GCBs moved according to motility behaviors B5-B7. This prediction matches the experimentally-observed motility behaviors of these cell types, suggesting that the measured Tfh and GCB motility enable maximal surveillance of the germinal center environment (**Figure 7I**). Our model further suggests that the dysregulation of Tfh motility towards slower motility behaviors can reduce the number of experienced unique Tfh interactions per GCB, providing a mechanism by which dysregulated cell motility may lead to diminished immune responses. In future work, we hope to run these simulations over longer durations and test how GCBs being confined to a volume representative of the light zone and Tfhs exploring unconfined volumes (representative of Tfh ability to move between multiple GCs) affect GCB-Tfh interactions.

Prior studies have leveraged computational modeling to understand how immune cell motility enables cell-cell interactions (22–25). Many prior models simulate immune cell motility as a persistent random walk (22–25) in which the average speed and persistence time (average time before cell changes direction) of lymphocytes was approximated from tracked trajectories from *in vivo* intravital microscopy videos. Here, we go further by quantifying several distinct motility behaviors from the *in vivo* intravital microscopy data, and then by finding mechanistic parameters that can recapitulate each of these distinct motility behaviors. Our approach allows us to model the intrinsic heterogeneity of cell motility behaviors, by modeling a single cell type as a collection of distinct motility behaviors based on experimental observations. Moreover, our stochastic model also can simulate the intrinsic variability within a single motility behavior. By using a distribution of probabilistic movement and turn probabilities, we can simulate a population of stochastic trajectories that mimic the heterogeneity in the population of experimentally-observed trajectories.

In this way, this pipeline provides a natural extension to prior modeling efforts that allow us to probe how heterogeneous motility patterns of B- and T-cells influence their ability to engage in cell-cell interactions that carry out the adaptive immune response.

We validated our simulation by running simulations that matched the density of labelled GCBs and Tfhs within each experimental intravital microscopy video, and testing whether the predicted number of interactions between labelled cells matched those observed in each video. Our simulation predictions were highly correlated with experimental measurements, which suggests that the key differences between experiments, such as labeled cell density, are being well accounted for; but generally under-predicted measured interactions by a factor of 2. We hypothesize that this under-prediction stems from the fact that our current model does not simulate how antigen-specific affinity between GCBs and Tfhs may prolong certain interactions. A Tfh that has a T-cell receptor with high affinity to the presented antigen by a GCB will experience a longer cell-cell interaction that would increase the number of total interactions measured in the experimental system.

Our current model only simulates how the movement of cells enable GCBs and Tfhs to encounter each other. In the future, we will incorporate rules that enable GCBs and Tfhs to also have affinity-driven interactions that would more accurately capture this behavior. This would not be a trivial addition; increasing interaction time would further affect the trajectories and thus the simulated motility patterns, and would result in needing to further refine the optimization of model movement parameters. Future work can also integrate our approach for simulating GCB and Tfh motility within spatially-resolved representations of the GC reaction that contain a follicular dendritic network that orients GCB and Tfh movement via chemotactic gradients. Several prior studies have modelled the interaction dynamics and spatial orientation of the germinal center reaction (26–31). In future work, we hope to integrate our model of heterogeneous cell motility with these computational models to further elucidate how distinct lymphocyte motility behaviors drive varied immune responses.

Cell motility drives cell-cell interactions that are critical for tissue function in several biological systems. The framework presented here is adaptable to understand how heterogeneous motility behaviors drive interactions in a variety of tissue systems under physiological and pathophysiological conditions.

ACKNOWLEDGEMENTS

We acknowledge the financial support for this work from the National Science Foundation Graduate Research Fellowship Program (to N.S.); the National Institutes of Health under award numbers R35GM157099 (to J.M.P.); and the 2024 Salisbury Family and Center for Innovative Medicine Human Aging Project (HAP) Scholar Award (to J.M.P.).

AUTHOR CONTRIBUTIONS

N.S., J.M.P., F.M.G., and W.B. conceived this study. K.C. and W.B. performed animal experiments, collected data, and contributed reagents. N.S., C.M., J.M.P., and F.M.G. conceived data analysis. N.S. and C.M. performed formal analysis. All authors interpreted results. N.S., J.M.P., and F.M.G. wrote manuscript. All authors contributed to reviewing and editing manuscript. J.M.P. and F.M.G. contributed equally as co-corresponding authors.

METHODS

We developed a data-driven simulation pipeline to 1) identify emergent cell motility behaviors based on three-dimensional (3D), *in vivo* intravital time-lapse microscopy and 2) simulate these single-cell motility behaviors within multi-cell simulations to predict how differential motility behaviors drive the likelihood of cell-cell interactions. Below, we discuss this pipeline in two parts. First, we discuss the experimental imaging setup and the data-driven analysis of experimental data to identify emergent motility behaviors that characterize single-cell trajectories. Then, we discuss the process of building and validating agent-based models (ABMs) to recapitulate single-cell motility behaviors within 3D volumes to predict cell-cell interaction likelihoods.

Mouse intravital microscopy system to image GCB and Tfh cell motility. To visualize lymphocytes within mouse germinal centers, fluorescently labelled T-follicular helper (Tfh) cells and germinal center B-cells (GCBs) were transferred via bone marrow transplant to recipient mice. After immune cell repopulation in recipient mice, germinal center (GC) responses were initiated based on standard procedures using NP-OVA injected into footpad (20). Two-photon intra-vital imaging of the cells within the popliteal lymph node was performed at the peak of the GC reaction between days 9 and 11. The imaging duration was 89.5 minutes at 30-second intervals (180 frames) and the imaging volume was 231 $\mu\text{m} \times 231 \mu\text{m} \times 90 \mu\text{m}$.

Bone marrow transplant. Fluorescently labelled cell populations were generated by crossing distinct female donor mice groups. Cy1-cre mice (#010611, The Jackson Laboratory) were crossed with R26-CFP (32) or R26R-EYFP mice (#006148, The Jackson Laboratory) to obtain GCBs fluorescently labelled with either CFP or YFP. CD4-Cre mice (#022071, The Jackson Laboratory) were mated with R26R-tdTomato mice (#007909, The Jackson Laboratory) to generate Tfhs fluorescently labelled with tdTomato. GCBs and Tfhs were harvested from the bone marrow of these donors at 8–12 weeks. Harvested cells were injected into C57BL/6J host female mice (#000664, The Jackson Laboratory) (450 rads the day before and 450 rads 2 hours before transplantation). Recipient mice were lethally irradiated with 450 rads the day before and 2 hours prior to transplantation.

Intravital two-photon microscopy. We performed intravital imaging of mouse popliteal lymph node GCs four to six months after bone marrow transplant. We prepared the popliteal lymph node for imaging based on previously established methods (20). Imaged mice received 1–1.5% isoflurane in oxygen for anesthetization. Prior to imaging, we shaved the leg skin using a shaver and hair removal cream (Nair). Using microdissection forceps, we made an incision behind the knee and removed fatty tissue covering the popliteal lymph node. We then hydrated the popliteal lymph node with saline and embedded the lymph node within a cover glass. We applied grease below the cover glass to prevent saline evaporation. We placed a heating wire (nickel-chromium) above the cover glass to maintain lymph node temperature at $36.5 \pm 0.5^\circ\text{C}$. We maintained the core body temperature of mouse at 36–37 $^\circ\text{C}$ using a temperature controller (FHC) that comprised a rectal probe and heating pad. We used a temperature probe (IT-23, Braintree Scientific) below the cover glass to monitor lymph node temperature.

We used a two-photon microscope (Bergamo II with ThorImage 4.1, Thorlabs) with a NA 1.05 objective (XLPLN25XWMP2, Olympus) for image acquisition. We used a mode-locked Ti:sapphire laser (Chameleon Vision-S, Coherent) as the excitation source. We used several band-pass filters to image CFP, YFP, and tdTomato simultaneously (FF01-475/42, FF03-525/50, FF01-585/29, FF01-623/32, Semrock). The imaging volume was 231 μm x 231 μm x 90 μm . We acquired images at 30-second intervals.

Data-driven analysis of trajectories from intravital time-lapse microscopy images. The overall pipeline for data-driven analysis of the intravital microscopy dataset includes 4 steps (Figure 2). First, we used the commercial software, IMARIS (Oxford Instruments) to segment and track single-cell trajectories within each set of time-lapse images. Second, we computed 36 motility features from each trajectory to quantify displacements and angular characteristics for each cell (Table 1). Third, we applied dimensionality reduction techniques (principal component analysis and factor analysis) to identify orthogonal features that differentiated patterns of trajectories within the dataset, and unsupervised clustering to define distinct motility behaviors. Finally, for quality control and noise reduction, we eliminated artifactual trajectories based on outlier feature values. We repeated clustering on the cleaned dataset. We expand upon each of these steps in detail in the following sub-sections.

Extraction of trajectories from intravital time-lapse microscopy images. To extract single-cell trajectories from each intravital time-lapse microscopy image set, IMARIS software was used to segment cells and track individual trajectories. A total of 9,720 cell trajectories were extracted from the videos of the 15 mice. We tracked trajectories that lasted at least 9.5 minutes (20 frames) and for consistency of comparison analyzed only nonoverlapping complete 20 frame sequences of these trajectories. We also segmented cells that were within the imaging volume for at least 2 minutes (5 frames) to estimate the density of labelled cells within the imaging volume. Throughout the text, we refer to “tracked” cells as cells that were tracked continuously for 20 frames and for which we derived a cell trajectory. We refer to “segmented” cells as those that were tracked continuously for at least 5 frames, and were a part of the “labelled” cell population measured within the image but not necessarily used to derive a motility trajectory. In IMARIS, we tracked the overlapping surface-to-surface volume of tracked cells with any segmented cells over time. We processed this metric to derive a binary state of cell-cell interaction, such that if the overlapping volume (continuous value) between two cells was greater than zero those two cells were considered to be interacting (binary state).

Motility feature extraction from each trajectory. For each of the 9,720 trajectories, we extracted 36 motility features to describe each trajectory (Table 1). These features describe the displacement and angular displacement aspects of the trajectory. To reduce the feature space prior to dimensionality reduction and unsupervised clustering, we applied a principal component analysis (PCA) and factor analysis. First, we identified how many principal components (PCs) explained approximately 75% of variance within the data. We then performed factor analysis to derive a communality score for features within the PC space that explains 75% of the variance in the data, and selected features with a communality score > 0.5 for clustering. The communality score measures how much each individual features contributes to the proportional variance

explained within the selected PC space. A communality score threshold of 0.5 was selected to identify features with significant contribution to the selected PC space.

Dimensionality reduction & unsupervised clustering of single-cell trajectories. For ease of visualization, we projected the motility features for each trajectory onto a two-dimensional UMAP embedding. To characterize how this UMAP embedding differentiated trajectories, we colored the UMAP space according to the value of each motility feature. We then applied unsupervised hierarchical clustering and k -means clustering on motility features (selected by factor analysis according to methods described in the previous section) to identify similar groups of cells/trajectories within the data. To phenotype each cluster, we plotted the distribution of key motility features across each cluster. In this process, we also identified clusters that had outlier values for certain motility features and re-examined trajectories within these clusters to assess whether these trajectories were appropriately segmented/tracked. Based on this process, we developed rules to eliminate outlier trajectories and repeated the steps of motility feature extraction, dimensionality reduction, and unsupervised clustering to identify and classify cells within discrete motility behaviors (see *Results* section *Initial trajectory clustering and Outlier elimination* and *Supplementary Text S1*).

Simulation overview. We developed a three-dimensional (3D) on-lattice agent-based model (ABM) to simulate single-cell motility behaviors and multicellular interactions. Cells are simulated as autonomous agents that evaluate a probabilistic decision to move at each simulated timestep in the ABM. Our on-lattice assumption assumes that the centers of cells can only move between the centers of neighboring voxels in our grid-based simulated environment. We conducted both single-cell and multi-cell simulations. Within single-cell simulations, cell agents move independently of environmental obstructions. In multi-cell simulations, cell agents consider additional rules that govern contact and overlap with surrounding cells. Below, we discuss the cell agent movement rule that dictates how cells move within the ABM environment. Then, we discuss nuances in the simulation environment and ruleset for single-cell and multi-cell simulations.

Cell agent movement rule. At each timestep, cell agents execute a motility rule governed by two parameters: the movement probability (*MP*) defines the probability of the cell moving to a neighboring voxel in the simulation space during one timestep; and the turn probability (*TP*) dictates whether the cell will change its heading during this movement. If the turn probability is not satisfied, the cell will move to the voxel ahead that it is already pointing to — i.e. the cell will move persistently. If the turn probability is satisfied, the cell will change its direction prior to moving (Figure 5A). Because turn behaviors only emerge when the cell decides to move, the effective likelihood of a cell turning is the product of *MP* and *TP*.

Single-cell simulations. Within single-cell (SC) simulations, cell agents evaluate *MP* and *TP* to move through the simulation environment without consideration for environmental obstructions, i.e. cells do not consider additional rules to prevent overlap with surrounding cells. Because cells do not need to apply volume exclusion rules ((unlike *multi-cell simulations*, see below)), single-cell simulations are more efficient to run than multi-cell simulations. Therefore, we initially used single-cell simulations to assess how *MP* and *TP* affect the motility features of simulated

trajectories. We then compared simulated trajectories from single-cell simulations with those from multi-cell simulations, to assess whether single-cell simulations can be used to fit model parameters (i.e. *MP* and *TP*) to recapitulate experimentally-observed motility behaviors.

In single-cell simulations, cells are seeded at the center of the simulation world with a random heading. The bounds of the simulated world size are set sufficiently large that the cell cannot escape the simulated environment during the runtime of the simulation. For example, if the simulation run time was 20 timesteps, the simulated world size spanned -20 to 20 voxels in the x, y, z directions. Each simulation was run for a constant *MP*, *TP* value with 500 cells to generate 500 trajectories per (*MP*, *TP*) combination.

Multi-cell simulations. The multi-cell simulations model multiple cellular agents within a simulation world. These simulations enable us to predict how cell density can affect cell trajectories. Moreover, this framework allows the model to detect cells making contact (interacting).

The multi-cell simulations include additional criteria to the cell movement rule to prevent cell-cell overlap. If a cell decides to move persistently and the voxel ahead is occupied, the cell searches for an empty voxel that neighbors both its current location and the neighboring voxel that the cell is pointing to. If any of these voxels are unoccupied, the cell moves to one of these locations chosen at random with equal likelihood; if all voxels are occupied, no movement occurs. This movement behavior allows cells to move around obstructions while maintaining somewhat persistent motion. This consideration is not necessary for a cell when it is turning because it already has several voxels to choose from that could be unoccupied.

In multi-cell simulations, cells are seeded at random locations in the simulation world with a random directional heading. Multi-cell simulations assume that we are simulating a representative subspace of the entire experimental system and apply periodic boundary conditions. Cells are allowed to wrap around the simulation world and maintain the same identity. This wrapping behavior assumes that the simulated space is a sub-volume of a larger relatively homogeneously distributed environment and, therefore, if a cell leaves the simulated space it would encounter an environment that is effectively similar to the one we are simulating. This assumption allows us to track individual cellular interactions over the entire duration of the simulation. This assumption also allows us to save computational resources by simulating a smaller volume than the experimental imaging volume. For select simulations, we run at exactly the imaging volume, to check that the smaller-world simulations are consistent. However, the computational cost of multicellular simulations far exceeds those for single cells, and this is why we use periodic assumptions to run smaller volumes but interpret them appropriately in relation to larger volumes. In addition, we ran some multi-cell simulations with the assumption that the simulated space was a confined volume. In confined volume simulations, when a cell leaves the imaging volume a new cell is spawned in the wrapped location to maintain cell density within the simulation. We will note in the results when we are using a confined volume, and how to interpret those simulations.

Spatiotemporal resolution of simulations. The experimental data we sought to recapitulate contained 3D single-cell trajectories that were 9.5 minutes in duration and collected for 20 consecutive frames (i.e. a temporal resolution of 30 seconds and a collection of 19 possible cell

movements). In our models, we had to determine what spatiotemporal resolution would best recapitulate the motility properties of the experimental data. The simplest solution for cellular ABMs is typically to assume a voxel size equal to the volume of the cell. But here, that assumption would confound the resolution of simulated trajectories, because it would assume that a cell could only move a cell-size distance per timestep, while in the experimental data the cells may move any number from a continuous range of distances between frames. If simulated cells can only move one cell-size distance at a time, the simulated trajectories may not capture fine-grained behaviors of slow-moving cells in our system.

To enable our simulations to capture behaviors of slow- and fast-moving cells we tested select voxel sizes from 1-10 μm and timestep sizes from 5-30 seconds, while keeping the overall duration of the simulation to 9.5 minutes. For each spatiotemporal resolution pair (voxel size, timestep size), we generated a simulated dataset of trajectories by co-varying *MP* and *TP* from 0 to 1. We then benchmarked the simulated trajectories against the experimental data by comparing the distributions of several motility features extracted from each trajectory. Based on this analysis, we chose a spatial resolution of 2 μm and a temporal resolution of 7.5 seconds (i.e. 76 time intervals or 77 timesteps), because this spatiotemporal resolution captures the range of all experimental motility parameter distributions.

Our simulation uses a voxel size of $8\mu\text{m}^3$ and a timestep of 7.5 seconds, and we assume that all cells have a uniform radius of 4 μm . The simulation voxel size is smaller than the cell size, and we apply volume exclusion rules to allow cells to interact but not to occupy the same space. To simulate the intercalation of cells as they move within a 3D environment, we simulate cells as having an effective minimum radius of 3 μm which allows cells to have up to 1 μm of overlap with each other, representing the deformability of cells as they contact and interact with each other.

Parameterization of simulation motility parameters to recapitulate experimental motility behaviors. We sought to parameterize our simulation to the distinct motility patterns that were derived in the experimental data using unsupervised clustering. We compared two approaches for model parameterization: a top-down, mixed modelling approach and bottom-up, nearest neighbors approach. Prior to applying each parameterization approach, we generated a “simulated trajectory space” by running simulations for different values of *MP* and *TP*. We sampled *MP* uniformly from 0.05 to 0.95 (19 unique *MP* values) and we sampled *TP* from 0 to 1, including higher resolution at small values ([0, 0.0005, 0.001, 0.005, 0.01, 0.025, 0.05, 0.1, 0.2, 0.3, 0.4, 0.5, 0.6, 0.7, 0.8, 0.9]; 16 unique *TP* values). We ran the parameterization algorithms on single-cell and multi-cell simulations. In single-cell simulations, 500 simulated trajectories were generated per (*MP*, *TP*) combination. Multi-cell simulations were run at a 0.5 cellular density (i.e. 50% of the volume occupied by cells) in a simulated cube that was 55 x 55 x 55 voxels, which yielded 2,482 simulated trajectories per simulation.

Top-down mixed modelling parameterization. In this approach, we quantified the sum of the squared minimum Euclidean distance between simulated trajectories in each (*MP*, *TP*) parameter combination and the experimental trajectories within each experimental motility pattern. We then used an evolutionary algorithm to find the optimal mixture of the (*MP*, *TP*) combinations that had

minimum aggregated distances within the 75th% of overall minimum aggregated distances (we chose to feed in only 75% of the data to exclude highly dissimilar parameter sets). The evolutionary algorithm first evaluated a set of initial guesses for the mixed distribution and iteratively improved these guesses by recombining choices that had high similarity to the experimental data.

Bottom-up, nearest-neighbors parameterization. In this parameterization approach, we first identify the k nearest neighbors in the simulated trajectory space to each experimental trajectory within an experimental motility pattern. We compute nearest neighbors using an Euclidean distance metric of 6 orthogonal features in the motility feature space (average speed, MSD ($\tau=2$), MSD ($\tau=2$) in the secondary axis, MSD ($\tau=2$) in the tertiary axis, progressivity, and net distance). Here τ denotes the time lag. We then extract the distribution of (MP , TP) parameter values that give rise to the simulated closest neighbors as the parameter distribution that recapitulates the experimental motility pattern of interest. If this distribution does not effectively recapitulate experimental trajectories, we re-weight the parameter distributions to selectively improve the fit for a given motility parameter. For example, if the nearest neighbors do not effectively recapitulate progressivity values, then we may need to re-weight the TP parameters of the nearest-neighbor (MP , TP) distribution. We select a threshold at which to re-weight TP and a proportion by which to re-weight the distribution—for example, we may choose to pick 80% of (MP , TP) combinations with a $TP > 0.7$ and 20% of (MP , TP) combinations with a $TP < 0.7$ to improve fit for a highly directed motility behavior. We used an evolutionary algorithm to optimize this threshold and re-weighting proportion. Based on comparison of this approach with top-down, mixture-modelling parameterization (described above), we found that this approach is less robust and did not choose to use this method (see *Supplementary Text S2*).

Quantification of simulated interaction dynamics. We extracted several features in the multi-cell ABM to characterize interaction dynamics. Assuming that all cells have a radius of 4 μm , we quantified interacting cells as those with a centroid-to-centroid distance of less than or equal to 8 μm . At each time step, we recorded each simulated cell's interacting neighbors. At the end of the simulation, we computed each cell's total number of interactions and total number of unique interactions. Unique interactions count the number of distinct cells interacted with, while total interactions count all interactions at all timesteps (i.e. total interactions could include interactions with the same cell that occur over multiple timesteps).

FIGURE CAPTIONS

Figure 1. Schematic of PRISMM pipeline with parallel analysis of experimental and computational data. (1) PRISMM first extracts single-cell GCB and Tfh trajectories from time-lapse, intravital imaging of *in vivo* mouse germinal centers. (2) From each lymphocyte trajectory, PRISMM calculates several motility features (Figure 2, Table 1). (3) PRISMM then applies unsupervised clustering on the multi-dimensional motility feature space to identify distinct motility behaviors (MBs). (4) In parallel, PRISMM uses a 3D, on-lattice agent-based model (ABM) to simulate cell motility based on parameters that control speed and tortuosity (move-probability (MP) and turn-probability (TP), respectively). This parameter space can be uniformly sampled to generate a universe of simulated trajectories. Because the model is stochastic, we simulate many trajectories per simulation parameter set. (5) We calculate the same motility features as in (2) from each simulated trajectory so that the simulated trajectories are directly comparable with experimental trajectories. (6) PRISMM then fits (MP, TP) parameter distributions to recapitulate each experimentally-observed motility behavior. To validate the ABM, (7) we run simulations that recapitulate the labelled densities of GCBs and Tfhs from each experimental video, and (8) test whether the simulation-predicted number of GCB-Tfh interactions, using the experimental cell densities as input, are comparable with measured interactions in each video. (9) Finally, we apply the mechanistic simulations to systematically explore how distinct motility behaviors drive GCB-Tfh interactions.

Figure 2. Schematic of quantification of motility features from each trajectory. (1) From the intravital microscopy data, we segmented and tracked 3D trajectories for individual GCBs and Tfhs. Each trajectory comprised the (x,y,z) coordinates of a single cell in 20 consecutive frames acquired at 30-second intervals. (2) For each experimental trajectory, we decomposed the trajectory into primary, secondary, and tertiary axes of movement. For the 3D trajectory, we quantified statistical features of the angular distribution. For the 3D trajectory and the trajectory decomposition, we quantified the following features: net distance and progressivity; statistical features of the displacement distribution; and the mean squared displacement at intervals of one, two, and three frames (30 seconds, 1-minute, and 1.5-minutes, respectively). (3) After extracting these features, we projected the multi-dimensional feature space into a UMAP embedding and applied unsupervised clustering to identify motility behaviors. We then examined the behavior of each motility cluster. (4) Finally, we eliminated possible outlier trajectories, and repeated step (3) on the cleaned dataset.

Figure 3. Quantification of distinct GCB and Tfh motility behaviors. **A**, Two-dimensional UMAP embedding of the motility features for GCB and Tfh trajectories (26 motility features per 6,912 trajectories). Lines on contour plots indicate 20% intervals of the cell populations. Embedding represents 3,184 Tfhs and 3,728 GCBs. All other UMAP projections shown in the figure correspond to this UMAP. **B**, Projection of standard-scaled average speed (top, left) and mean squared displacement at 1-minute intervals (bottom, left) onto UMAP embedding. Corresponding boxplots of average speed (top, right) and mean-squared displacement (bottom,

right) for each cell type. **C**, Projection of raw progressivity values (top, left) and standard-scaled net distance (bottom, left) onto UMAP embedding. Corresponding boxplots of progressivity (top, right) and net distance (bottom, right) distribution for each cell type. **D**, Heatmap representing standard-scaled values of each motility feature (26 rows) for each experimentally-observed trajectory (6,912 columns). Rows and columns are hierarchically clustered using Euclidean distance and Ward linkage. **E**, Projection of two motility classes (C1, C2) derived from hierarchical clustering onto the UMAP embedding. **F**, Boxplots of average speed (top) and progressivity (bottom) values for each motility class. **G**, Count of each motility class within each cell type (left) and proportion of each cell type within each motility class (right). **H**, Heatmap representing standard-scaled values of each motility feature (rows) for each experimentally-observed trajectory (columns). Rows are hierarchically clustered using Euclidean distance and Ward linkage. Trajectories are ordered by *k-means* cluster label. *k-means* cluster label is shown on the top color band and motility class identity is shown on the bottom color band. **I**, Projection of seven motility behaviors (B1-B7) derived from *k-means* clustering onto the UMAP embedding. **J**, Boxplots of average speed and progressivity value distribution for each motility behavior. All comparisons were statistically significant ($p<0.05$) except for those marked by “n.s.”. **K**, Representative trajectories for each motility behavior (left-most). Proportion of each motility behavior within each cell type (left heatmap) and proportion of each cell type within each motility behavior (right bar plot). Statistical testing shown on boxplots with multiple groups indicate results from a Kruskal-Wallis test followed up with a Dunn test for post-hoc comparisons. Statistical testing shown on boxplots indicate results from a Mann-Whitney test. * indicates $p<0.05$, ** indicates $p<0.01$, and *** indicates $p<0.001$.

Figure 4. Calibrating single-cell ABMs to recapitulate experimentally-observed motility behaviors. **A**, Flowchart describing the process for developing the ABM that PRISMM employs to mechanistically simulate experimentally-observed motility behaviors. **B-E**, Heatmaps representing average values across 500 trajectories generated per (*MP*, *TP*) combination for the following motility features: average speed (**B**), mean squared displacement at 1-minute intervals (**C**), progressivity (**D**), and net distance (**E**). **F**, Heatmaps representing the number of motility features (out of 26 total) for which the simulated range encompassed the experimental range, at different spatial and temporal resolutions. **G**, The average proportion of the experimental range captured by the simulated range across 26 features, at different spatial and temporal resolutions. **H**, The \log_2 of the average ratio between the simulated range and experimental range across all 26 features for each spatial and temporal resolution. **I**, Heatmaps representing the aggregated minimum distance between the 500 simulated trajectories for each (*MP*, *TP*) parameter set and the experimentally-observed trajectories within each experimental motility behavior. **J**, Heatmaps representing the optimized mixed proportions of (*MP*, *TP*) parameter sets to recapitulate each experimentally-observed motility behavior. **K-N**, Boxplots comparing motility feature distributions for each motility behavior between the experimentally-observed trajectories (“E”), simulated trajectories in the closest (*MP*, *TP*) parameter set (“S1”), simulated trajectories in the optimized mixed distribution of (*MP*, *TP*) parameter sets (“S2”), and simulated trajectories from multi-cell simulations re-sampling this parameterization (“S3”), for the following motility features: average speed (**K**), mean squared displacement at 1-minute intervals (**L**), progressivity (**M**), and net

distance (**N**). * indicates that distribution has a Cohen's D value > 0.5 when compared with experimental distribution.

Figure 5. Comparing multi-cell ABM with single-cell ABM & calibration of multi-cell ABM to recapitulate experimentally-observed motility behaviors. **A**, Schematic of ABM ruleset for cell-agent movement in single-cell simulations versus multi-cell simulations that require considerations for avoiding obstructions. **B-E**, Heatmaps representing the average value across 2,482 simulated trajectories per (*MP*, *TP*) combination in the multi-cell simulation (left) and the log₂ fold change between this average and that for trajectories from the single-cell simulation (right) for the following motility features: average speed (**B**), mean squared displacement at 1-minute intervals (**C**), progressivity (**D**), and net distance (**E**). **F**, Heatmaps representing the aggregated minimum distance between the 2,482 simulated trajectories for each (*MP*, *TP*) parameter set in the multi-cell ABM and the experimentally-observed trajectories within each experimental motility behavior. **G**, Heatmaps representing the optimized mixed proportions of (*MP*, *TP*) parameter sets to recapitulate each experimentally-observed motility behavior. **H-K**, Boxplots comparing motility feature distributions for each motility behavior between the experimentally-observed trajectories ("E"), simulated trajectories in the closest (*MP*, *TP*) parameter set ("S1"), simulated trajectories in the optimized mixed distribution of (*MP*, *TP*) parameter sets ("S2"), and simulated trajectories from multi-cell simulations re-sampling this parameterization ("S3") for the following motility features: average speed (**H**), mean squared displacement at 1-minute intervals (**I**), progressivity (**J**), and net distance (**K**). * indicates that distribution has a Cohen's D value > 0.5 when compared with experimental distribution.

Figure 6. Validation of ABM predictions of GCB-Tfh interactions. **A**, Bar plot representing fractional volume of segmented and tracked cell types within each intravital microscopy experiment. Segmented cells refer to cells that were tracked for 5 continuous frames. Tracked cells refer to cells that were tracked for 20 continuous frames. **B**, Measured GCB-Tfh interactions in each intravital microscopy experiment. We measured interactions by processing the metric of volumetric overlap ratio between each tracked cell and any labelled cell type (which could have also been tracked for 20 frames or segmented for a minimum of 5 frames, see *Methods*). **C**, Scatter plot of simulation predictions against experimental measurements for total Tfh interactions per GCB. Vertical errorbars represent the standard deviation from 100 simulation repetitions. Line indicates a linear regression with the intercept fixed at zero. **D**, Scatter plots of simulation predictions against experimental measurements for total GCB interactions per Tfh. Vertical errorbars represent the standard deviation from 100 simulation repetitions. Line indicates a linear regression with the intercept fixed at zero. **E**, Bar plot representing the log₂ fold change between simulation predictions and experimental measurements for total Tfh interactions per GCB (blue) or total GCB interactions per Tfh (red). 'RMSE': root mean squared error between average simulation predictions and experimental measurements, 'r': r-value for Spearman correlation, 'p': p-value for Spearman correlation.

Figure 7. Application of ABM to predict how motility behavior drives unique GCB-Tfh interactions. A-D, Heatmaps representing **(A)** unique Tfh interactions per GCB, **(B)** unique GCB interactions per Tfh, **(C)** total Tfh interactions per GCB, and **(D)** total GCB interactions per Tfh when running confined-volume simulations in which Tfhs and GCBs follow each experimentally-observed motility behavior (B1-B7). Each simulation volume was 40% occupied by GCBs and 10% occupied by Tfhs. The simulation world dimensions were 110 x 110 x 110 μm and simulated a confined volume with constant density by allowing cell agents to leave the simulation world and spawning new cells at simulation boundaries whenever a cell agent leaves the world (see *Methods*). **E-H,** Heatmaps representing unique Tfh interactions per GCB **(E)**, unique GCB interactions per Tfh **(F)**, total Tfh interactions per GCB **(G)**, and total GCB interactions per Tfh **(H)** when running unconfined-volume simulations in which Tfhs and GCBs follow each experimentally-observed motility behavior (B1-B7). Each simulation volume was 40% occupied by GCBs and 10% occupied by Tfhs. The simulation world dimensions were 110 x 110 x 110 μm and simulated an unconfined volume with constant density by allowing cell agents to leave the simulation world and re-enter as the same cell agent (see *Methods*). **I,** Schematic describing that the simulation suggests that Tfhs moving fast and directly maximize unique interactions with GCBs moving slowly and tortuously within local environments of the GC light zone.

TABLES

Table 1. Motility features computed for experimental and simulated trajectories. Each described feature was computed for each trajectory. Included features are highlighted green. Criteria for excluded features are described.

Feature	Description	Axis	Included/Exclusion criteria
Average angular displacement (rad/minute)	Mean of the angular displacement distribution	3D	
Angular displacement skewness	Skewness of the angular displacement distribution	3D	< 50% communality score
Angular displacement kurtosis	Kurtosis of the angular displacement distribution	3D	High kurtosis tended to emerge due to low sampling frequency (Supplementary Figure 3B)
Net distance (μm)	Resultant distance between first and last point	3D A1 A2 A3	
Progressivity	Ratio of total distance to net distance	3D A1 A2 A3	
Average speed ($\mu\text{m}/\text{minute}$)	Mean of the displacement distribution	3D A1 A2 A3	
Displacement skewness	Skewness of the displacement distribution	3D A1 A2 A3	< 50% communality score
Displacement kurtosis	Kurtosis of the displacement distribution	3D A1 A2 A3	High kurtosis tended to emerge due to low sampling frequency (Supplementary Figure 3B)
Alpha ($\mu\text{m}^2 / \text{minute}$)	Slop of the Mean Squared Displacement v. Time interval function.	3D	
Mean squared displacement, $T = 1$ (μm^2)	Mean of the squared displacements between trajectory frames separated by one acquisition intervals.	3D A1 A2 A3	
		3D	

Mean squared displacement, $T = 2 \text{ } (\mu\text{m}^2)$	Mean of the squared displacements between trajectory frames separated by two acquisition intervals.	A1	
		A2	
		A3	
Mean squared displacement, $T = 3 \text{ } (\mu\text{m}^2)$	Mean of the squared displacements between trajectory frames separated by three acquisition intervals.	3D	
		A1	
		A2	
		A3	

REFERENCES

1. Maity D, Sivakumar N, Kamat P, Zamponi N, Min C, Du W, et al. Profiling Dynamic Patterns of Single-Cell Motility. *Adv Sci [Internet]*. 2024 [cited 2024 Dec 4];11(38):2400918. Available from: <https://onlinelibrary.wiley.com/doi/abs/10.1002/advs.202400918>
2. De la Fuente IM, Carrasco-Pujante J, Camino-Pontes B, Fedetz M, Bringas C, Pérez-Samartín A, et al. Systemic cellular migration: The forces driving the directed locomotion movement of cells. *PNAS Nexus [Internet]*. 2024 May 1 [cited 2024 May 29];3(5):pgae171. Available from: [https://livejohnshopkins-my.sharepoint.com/personal/nsivaku3_jh_edu/Documents/Notebooks/Research%20-%20Linked%20Files/s41590-021-01101-1%20\(1\).pdf](https://livejohnshopkins-my.sharepoint.com/personal/nsivaku3_jh_edu/Documents/Notebooks/Research%20-%20Linked%20Files/s41590-021-01101-1%20(1).pdf)
3. Krummel MF, Bartumeus F, Gérard A. T cell migration, search strategies and mechanisms. *Nat Rev Immunol [Internet]*. 2016 Mar [cited 2025 Jun 20];16(3):193–201. Available from: <https://www.nature.com/articles/nri.2015.16>
4. Yamada KM, Sixt M. Mechanisms of 3D cell migration. *Nat Rev Mol Cell Biol [Internet]*. 2019 Dec [cited 2025 Jun 20];20(12):738–52. Available from: <https://www.nature.com/articles/s41580-019-0172-9>
5. SenGupta S, Parent CA, Bear JE. The principles of directed cell migration. *Nat Rev Mol Cell Biol [Internet]*. 2021 Aug [cited 2025 Jun 20];22(8):529–47. Available from: <https://www.nature.com/articles/s41580-021-00366-6>
6. Victora GD, Nussenzweig MC. Germinal Centers. *Annu Rev Immunol [Internet]*. 2022 Apr 26 [cited 2024 Jun 17];40(Volume 40, 2022):413–42. Available from: <https://www.annualreviews.org/content/journals/10.1146/annurev-immunol-120419-022408>
7. Mesin L, Ersching J, Victora GD. Germinal Center B Cell Dynamics. *Immunity [Internet]*. 2016 Sep 20 [cited 2024 Jun 6];45(3):471–82. Available from: https://livejohnshopkins-my.sharepoint.com/:b/r/personal/nsivaku3_jh_edu/Documents/OneNote%20Uploads/1-s2.0-S1074761316303454-main.pdf?csf=1&web=1&e=PihO7m
8. Stebegg M, Kumar SD, Silva-Cayetano A, Fonseca VR, Linterman MA, Graca L. Regulation of the Germinal Center Response. *Front Immunol [Internet]*. 2018 Oct 25 [cited 2025 Jun 20];9. Available from: <https://www.frontiersin.org/journals/immunology/articles/10.3389/fimmu.2018.02469/full>
9. Nakagawa R, Calado DP. Positive Selection in the Light Zone of Germinal Centers. *Front Immunol [Internet]*. 2021 Mar 31 [cited 2025 Jun 20];12. Available from: <https://www.frontiersin.org/journals/immunology/articles/10.3389/fimmu.2021.661678/full>
10. Vinuesa CG, Linterman MA, Goodnow CC, Randall KL. T cells and follicular dendritic cells in germinal center B-cell formation and selection. *Immunol Rev*. 2010 Sep;237(1):72–89.
11. Fleischmann E, Middelkamp V, van den Broek T. Deciphering the Human Germinal Center: A Review of Models to Study T–B Cell Interactions. *Eur J Immunol [Internet]*. 2025 [cited 2025 Jun 20];55(2):e202451460. Available from: <https://onlinelibrary.wiley.com/doi/abs/10.1002/eji.202451460>

12. Delgado M, Lennon-Duménil AM. How cell migration helps immune sentinels. *Front Cell Dev Biol* [Internet]. 2022 Oct 4 [cited 2025 Jun 20];10:932472. Available from: <https://www.ncbi.nlm.nih.gov/pmc/articles/PMC9577558/>
13. Miller MJ, Wei SH, Parker I, Cahalan MD. Two-Photon Imaging of Lymphocyte Motility and Antigen Response in Intact Lymph Node. *Science* [Internet]. 2002 Jun 7 [cited 2025 Jun 18];296(5574):1869–73. Available from: <https://www.science.org/doi/full/10.1126/science.1070051>
14. Stoll S, Delon J, Brotz TM, Germain RN. Dynamic Imaging of T Cell-Dendritic Cell Interactions in Lymph Nodes. *Science* [Internet]. 2002 Jun 7 [cited 2025 Jun 18];296(5574):1873–6. Available from: <https://www.science.org/doi/full/10.1126/science.1071065>
15. Boussou P, Bhakta NR, Lewis RS, Robey E. Dynamics of Thymocyte-Stromal Cell Interactions Visualized by Two-Photon Microscopy. *Science* [Internet]. 2002 Jun 7 [cited 2025 Jun 18];296(5574):1876–80. Available from: <https://www.science.org/doi/full/10.1126/science.1070945>
16. Batista FD, Dustin ML. Cell:cell interactions in the immune system. *Immunol Rev* [Internet]. 2013 [cited 2024 Dec 4];251(1):7–12. Available from: <https://onlinelibrary.wiley.com/doi/abs/10.1111/imr.12025>
17. Richner JM, Gmyrek GB, Govero J, Tu Y, Windt GJW van der, Metcalf TU, et al. Age-Dependent Cell Trafficking Defects in Draining Lymph Nodes Impair Adaptive Immunity and Control of West Nile Virus Infection. *PLOS Pathog* [Internet]. 2015 Jul 23 [cited 2024 Jul 26];11(7):e1005027. Available from: <https://journals.plos.org/plospathogens/article?id=10.1371/journal.ppat.1005027>
18. Reimer D, Meyer-Hermann M, Rakhytmzhan A, Steinmetz T, Tripal P, Thomas J, et al. B Cell Speed and B-FDC Contacts in Germinal Centers Determine Plasma Cell Output via Swiprosin-1/EFhd2. *Cell Rep* [Internet]. 2020 Aug [cited 2024 Jun 7];32(6):108030. Available from: <https://linkinghub.elsevier.com/retrieve/pii/S2211124720310159>
19. Germain RN, Robey EA, Cahalan MD. A Decade of Imaging Cellular Motility and Interaction Dynamics in the Immune System. *Science* [Internet]. 2012 Jun 29 [cited 2024 Dec 4];336(6089):1676–81. Available from: <https://www.science.org/doi/10.1126/science.1221063>
20. Choe K, Hontani Y, Wang T, Hebert E, Ouzounov DG, Lai K, et al. Intravital three-photon microscopy allows visualization over the entire depth of mouse lymph nodes. *Nat Immunol* [Internet]. 2022 Feb [cited 2024 May 29];23(2):330–40. Available from: <https://www.nature.com/articles/s41590-021-01101-1>
21. Pizzagalli DU, Farsakoglu Y, Palomino-Segura M, Palladino E, Sintes J, Marangoni F, et al. Leukocyte Tracking Database, a collection of immune cell tracks from intravital 2-photon microscopy videos. *Sci Data* [Internet]. 2018 Jul 17 [cited 2025 Jun 18];5(1):180129. Available from: <https://www.nature.com/articles/sdata2018129>
22. Preston SP, Waters SL, Jensen OE, Heaton PR, Pritchard DI. T-cell motility in the early stages of the immune response modeled as a random walk amongst targets. *Phys Rev E* [Internet]. 2006 Jul 17 [cited 2025 May 16];74(1):011910. Available from: <https://link.aps.org/doi/10.1103/PhysRevE.74.011910>

23. Nicholson D, Nicholson LB. A simple immune system simulation reveals optimal movement and cell density parameters for successful target clearance. *Immunology* [Internet]. 2008 [cited 2025 May 16];123(4):519–27. Available from: <https://onlinelibrary.wiley.com/doi/abs/10.1111/j.1365-2567.2007.02721.x>
24. Simulating T-cell motility in the lymph node paracortex with a packed lattice geometry - Bogle - 2008 - *Immunology & Cell Biology* - Wiley Online Library [Internet]. [cited 2025 May 16]. Available from: <https://onlinelibrary.wiley.com/doi/full/10.1038/icb.2008.60>
25. Frascoli F, Flood E, Kim PS. A model of the effects of cancer cell motility and cellular adhesion properties on tumour-immune dynamics. *Math Med Biol J IMA* [Internet]. 2017 Jun 1 [cited 2025 May 16];34(2):215–40. Available from: <https://doi.org/10.1093/imammb/dqw004>
26. Robert PA, Rastogi A, Binder SC, Meyer-Hermann M. How to Simulate a Germinal Center. *Methods Mol Biol* Clifton NJ. 2017;1623:303–34.
27. Bogle G, Dunbar PR. Agent-based simulation of T-cell activation and proliferation within a lymph node. *Immunol Cell Biol* [Internet]. 2010 [cited 2025 May 16];88(2):172–9. Available from: <https://onlinelibrary.wiley.com/doi/abs/10.1038/icb.2009.78>
28. Bogle G, Dunbar PR. On-Lattice Simulation of T Cell Motility, Chemotaxis, and Trafficking in the Lymph Node Paracortex. *PLOS ONE* [Internet]. 2012 Sep 19 [cited 2025 May 16];7(9):e45258. Available from: <https://journals.plos.org/plosone/article?id=10.1371/journal.pone.0045258>
29. Pae J, Schwan N, Ottino-Loffler B, DeWitt WS, Garg A, Bortolatto J, et al. Transient silencing of hypermutation preserves B cell affinity during clonal bursting. *Nature*. 2025 May;641(8062):486–94.
30. Schips M, Mitra T, Bandyopadhyay A, Meyer-Hermann M. Suppressive might of a few: T follicular regulatory cells impede auto-reactivity despite being outnumbered in the germinal centres. *Front Immunol*. 2023;14:1253704.
31. Garg AK, Mitra T, Schips M, Bandyopadhyay A, Meyer-Hermann M. Amount of antigen, T follicular helper cells and affinity of founder cells shape the diversity of germinal center B cells: A computational study. *Front Immunol*. 2023;14:1080853.
32. Srinivas S, Watanabe T, Lin CS, William CM, Tanabe Y, Jessell TM, et al. Cre reporter strains produced by targeted insertion of EYFP and ECFP into the ROSA26 locus. *BMC Dev Biol*. 2001;1:4.
33. Béguelin W, Teater M, Gearhart MD, Fernández MTC, Goldstein RL, Cárdenas MG, et al. EZH2 and BCL6 Cooperate to Assemble CBX8-BCOR Complex to Repress Bivalent Promoters, Mediate Germinal Center Formation and Lymphomagenesis. *Cancer Cell* [Internet]. 2016 Aug 8 [cited 2025 Jul 25];30(2):197–213. Available from: [https://www.cell.com/cancer-cell/abstract/S1535-6108\(16\)30337-3](https://www.cell.com/cancer-cell/abstract/S1535-6108(16)30337-3)

Intravital imaging

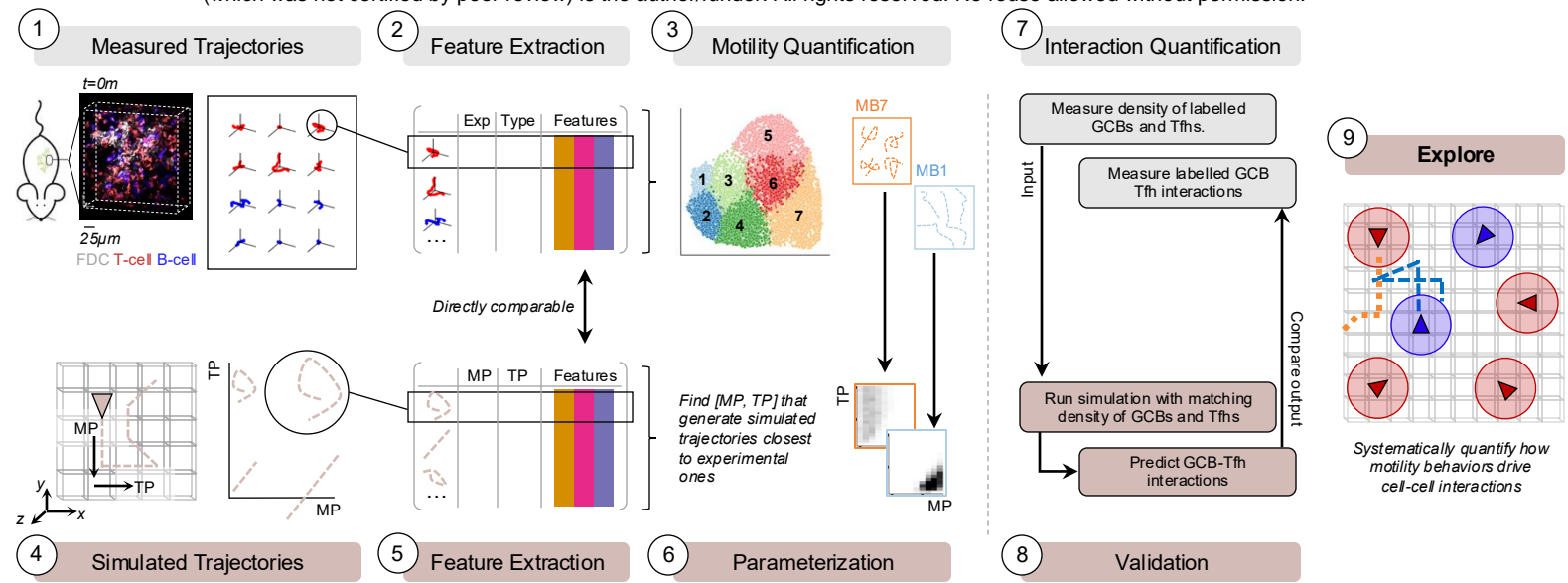
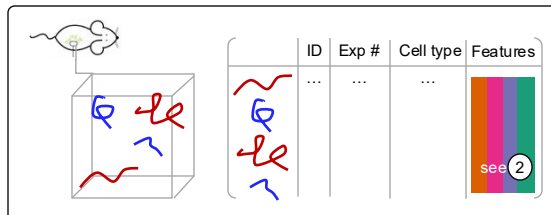
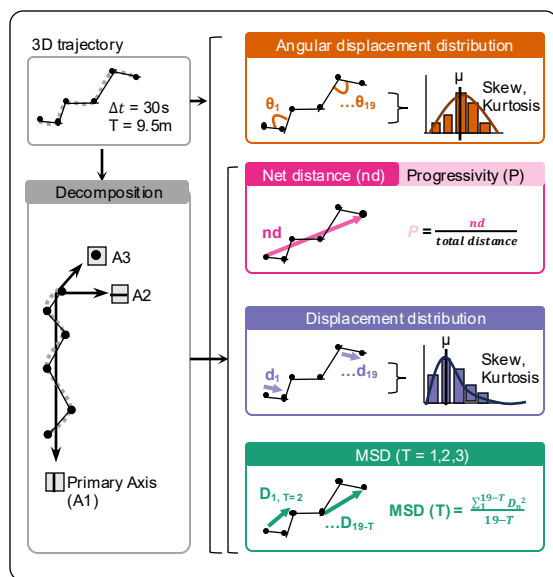


Figure 1. Schematic of PRISMM pipeline with parallel analysis of experimental and computational data.

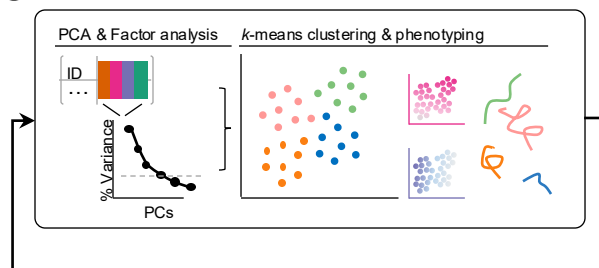
① Trajectory capture, extraction & registration



② Trajectory decomposition & feature extraction



③ Feature selection & Unsupervised clustering



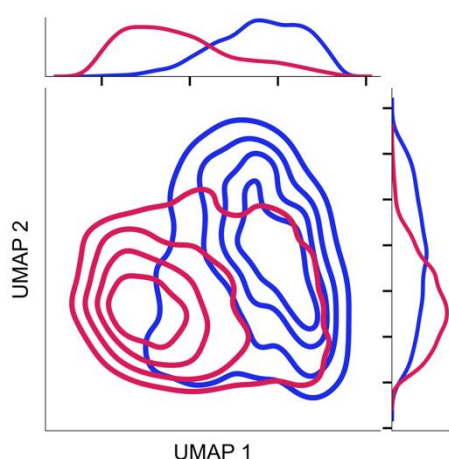
④ Outlier detection & Trajectory elimination

Figure 2. Schematic of quantification of motility features from each trajectory.

A

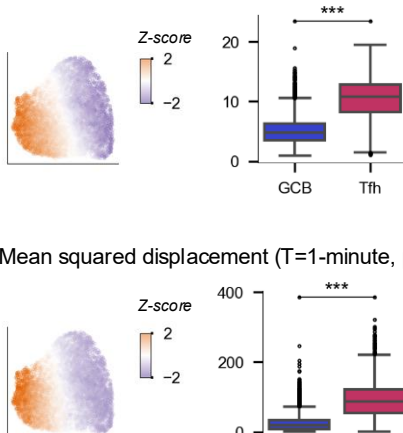
Experimental Motility Phenotypes
by Cell Type

■ Tfh ■ GCB



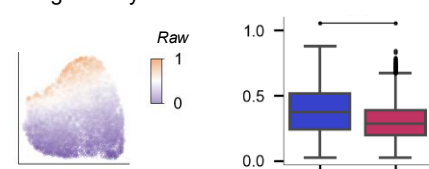
Displacement features

Average speed ($\mu\text{m}/\text{min}$)

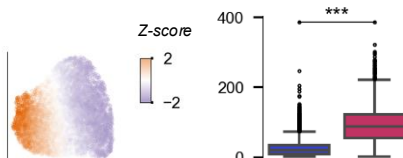


Tortuosity features

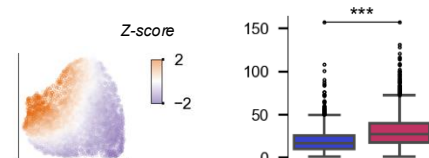
Progressivity



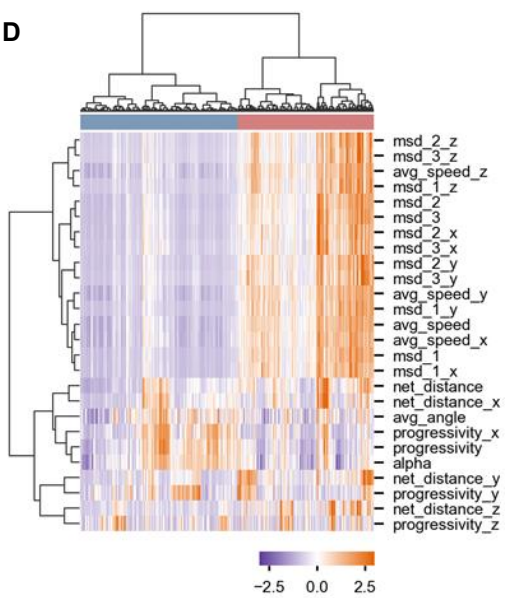
Mean squared displacement ($T=1\text{-minute}$, μm^2)



Net distance (μm)

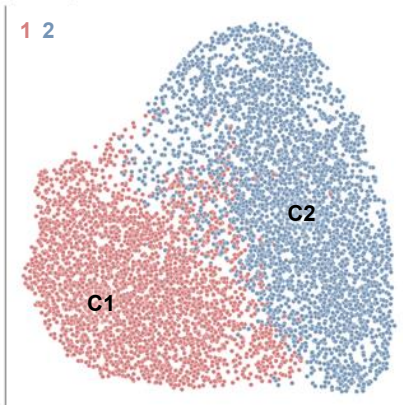


D



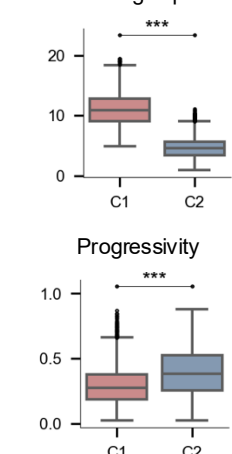
E

Motility classes
(hc = 2)

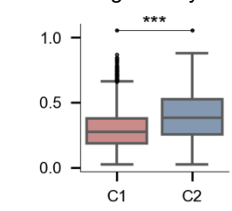


F

Average speed

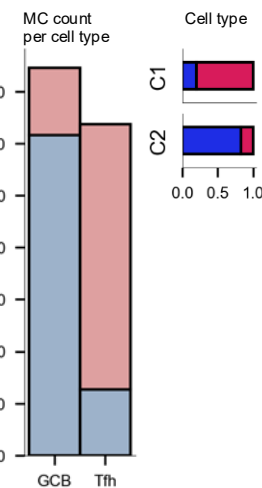


Progressivity

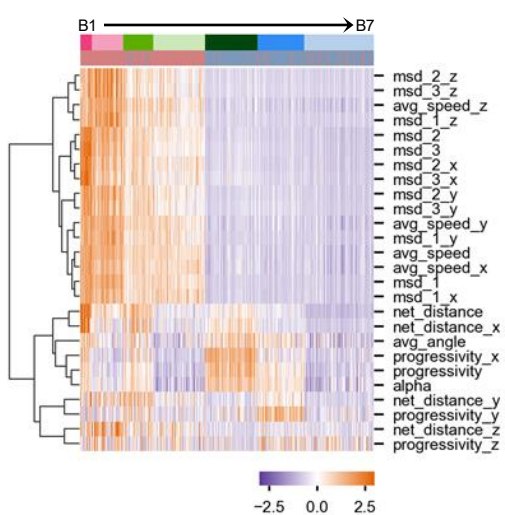


G

Occurrence of motility classes

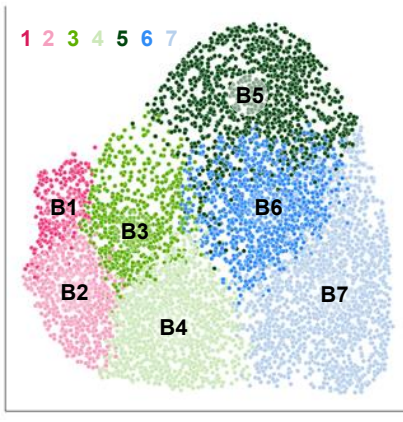


H



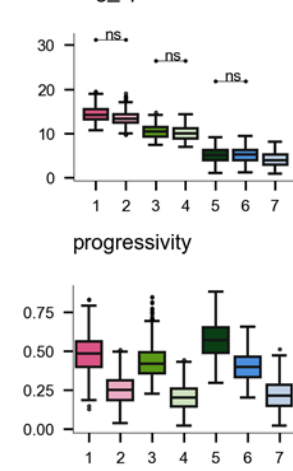
I

Experimental motility behaviors
(k = 7)

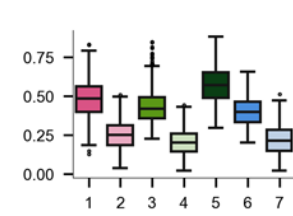


J

avg_speed



progressivity



K

Occurrence

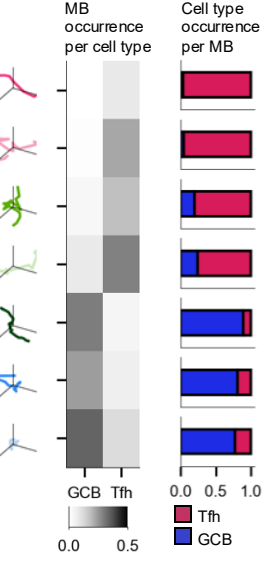


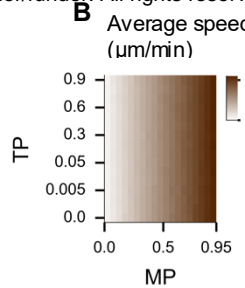
Figure 3. Quantification of distinct GCB and Tfh motility behaviors.

A

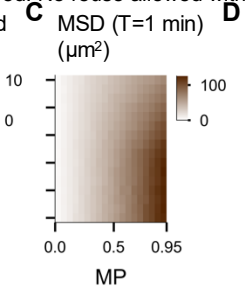
PRISMM Pipeline

- 1 Simulate Trajectory Sets for Different (MP, TP) Combinations & Spatiotemporal resolutions.
 - 2 Calibrate Spatiotemporal Resolution such that Model can Simulate the Range of all Experimental Motility Features.
 - 3 Within the Calibrated Spatiotemporal Resolution, Optimize (MP, TP) Parameter Regimes that Recapitulate each Experimental Motility Behavior.
- Count
- Motility feature value
- Simulation range
- Experimental range
- Pick spatiotemporal resolution for which simulation range matches experimental range for all motility features

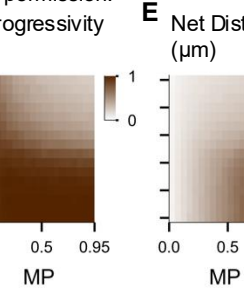
B



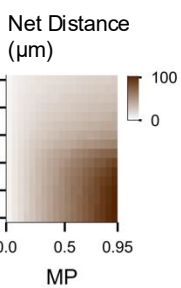
C



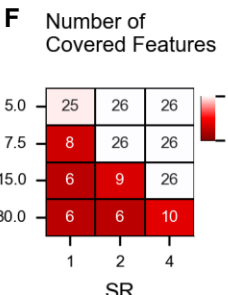
D



E



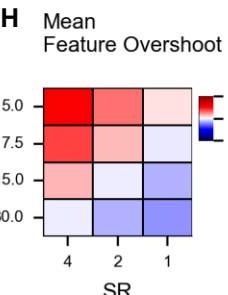
F



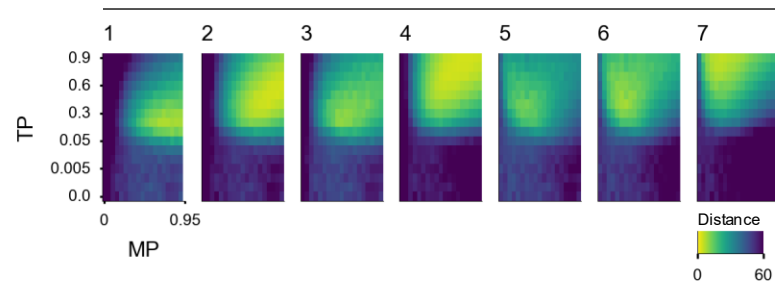
G



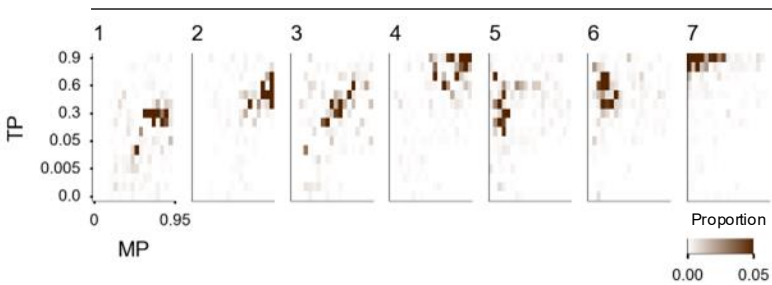
H



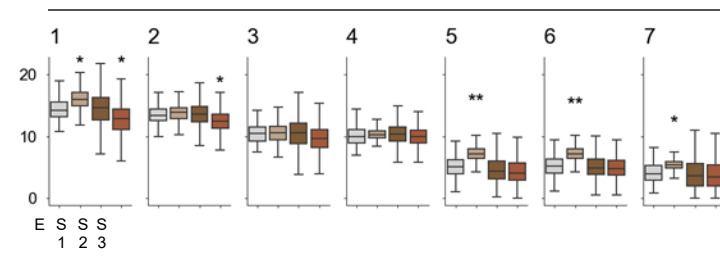
I Aggregated Minimum Distance Between each (MP, TP) Combination of Single-cell Simulated Trajectories & Each Experimental MB



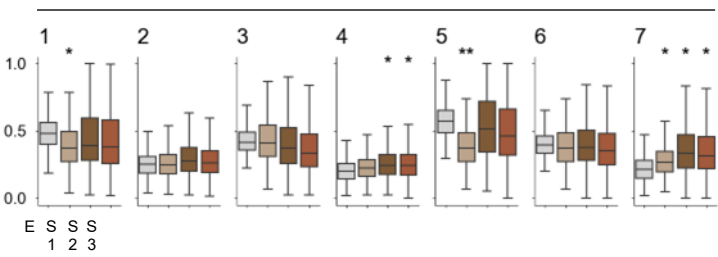
J Optimized Mixed Distribution of (MP, TP) Combinations from Single-Cell Simulations for each Experimental MB



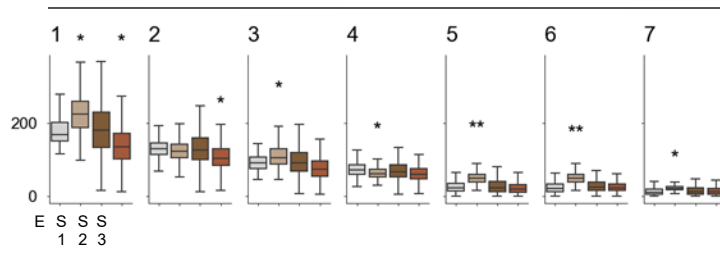
K Average speed ($\mu\text{m}/\text{min}$)



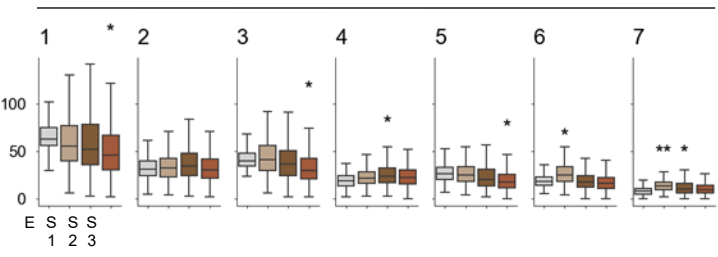
L Progressivity



M MSD ($T=1 \text{ min}$) (μm^2)



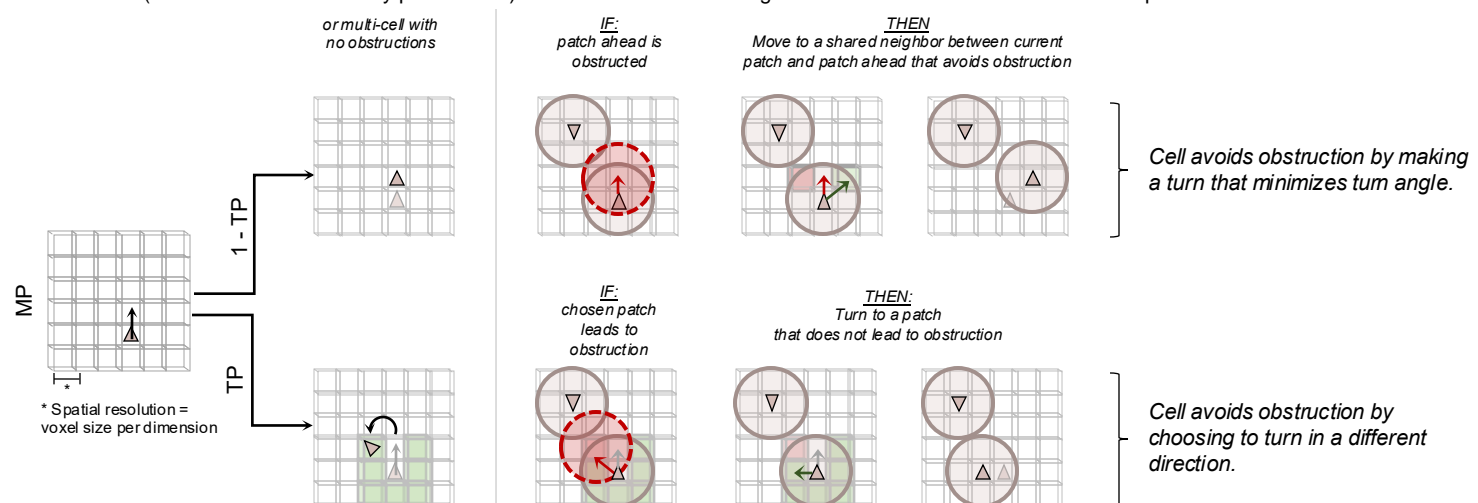
N Net Distance (μm)



(E) Experimental trajectories
(S1) SC simulated trajectories that sample the closest (MP, TP) distribution
(S2) SC simulated trajectories that sample mixed distribution
(MC) MC simulated trajectories that sample mixed distribution

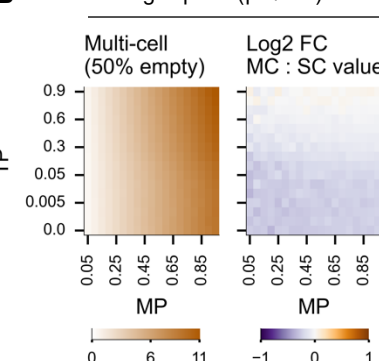
Figure 4. Calibrating single-cell ABMs to recapitulate experimentally-observed motility behaviors.

A

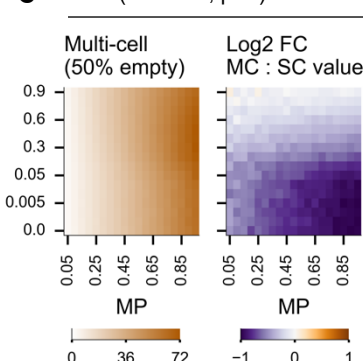


B

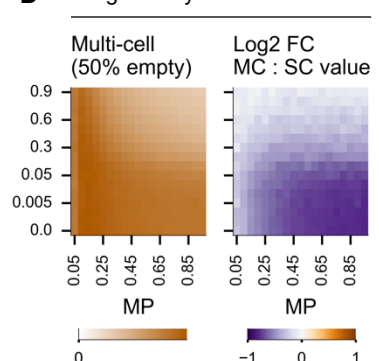
Average speed ($\mu\text{m}/\text{min}$)



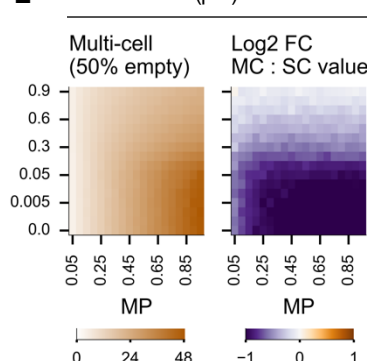
MSD ($T = 1\text{ min}$, μm^2)



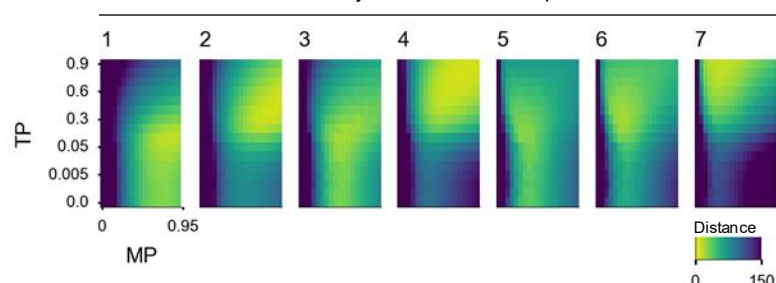
Progressivity



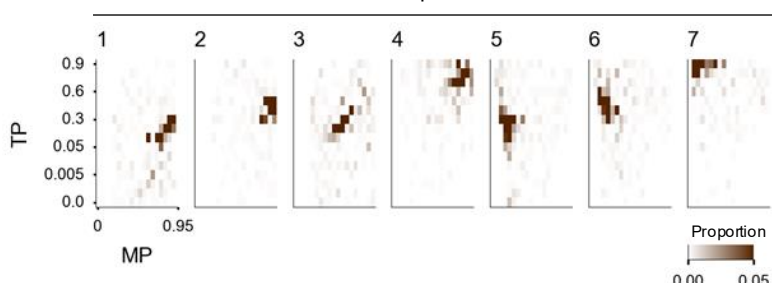
Net distance (μm)



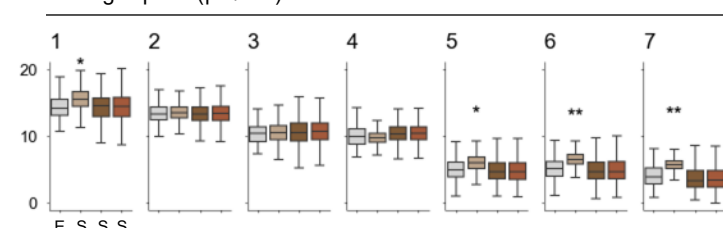
F Aggregated Minimum Distance Between each (MP, TP) Combination of Multi-cell Simulated Trajectories & Each Experimental MB



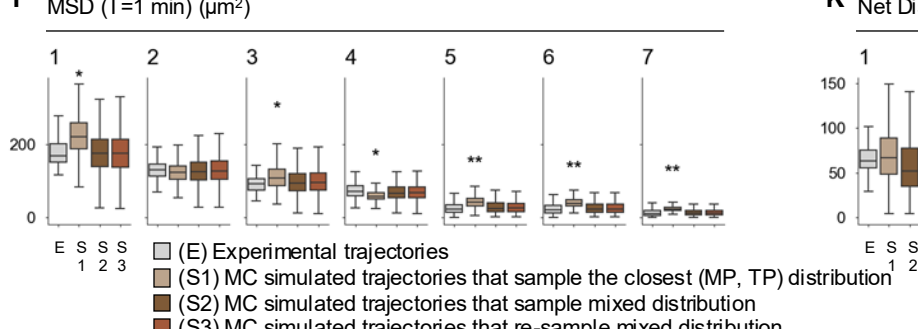
G Optimized Mixed Distribution of (MP, TP) Combinations from Multi-Cell Simulations for each Experimental MB



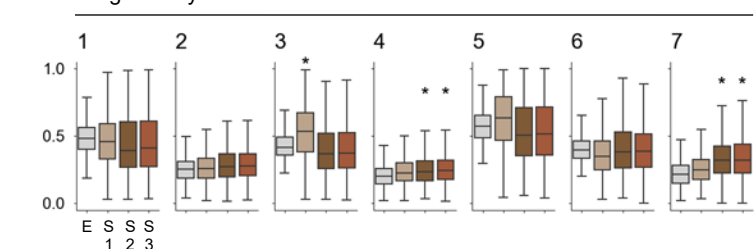
H Average speed ($\mu\text{m}/\text{min}$)



I MSD ($T=1\text{ min}$) (μm^2)



J Progressivity



K Net Distance (μm)

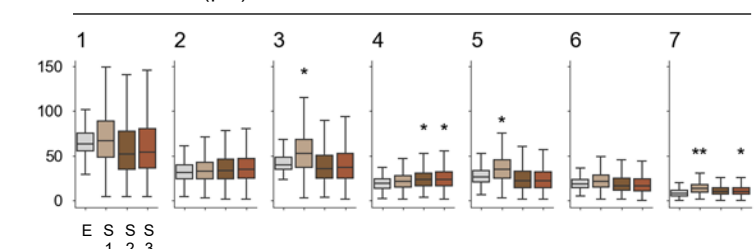


Figure 5. Comparing multi-cell ABM with single-cell ABM & calibration of multi-cell ABM to recapitulate experimentally-observed motility behaviors.

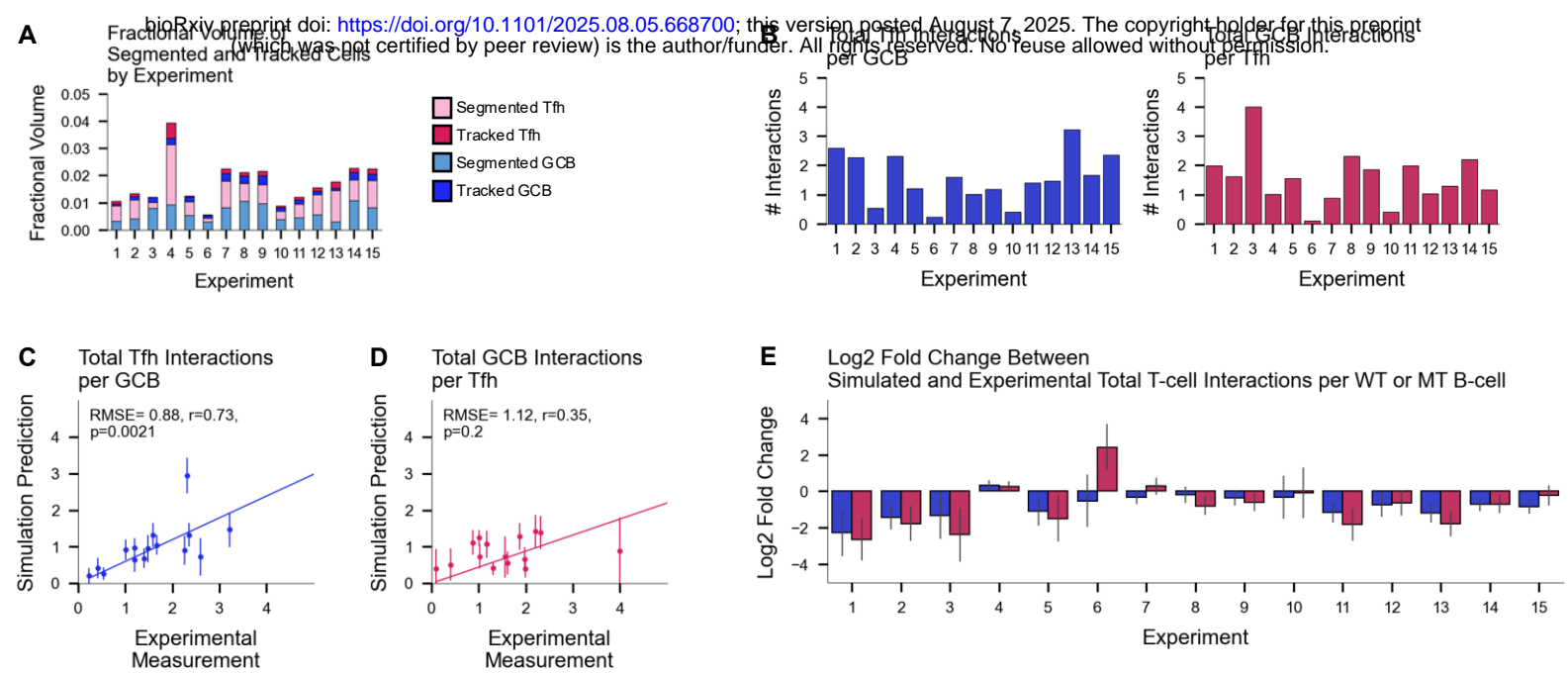
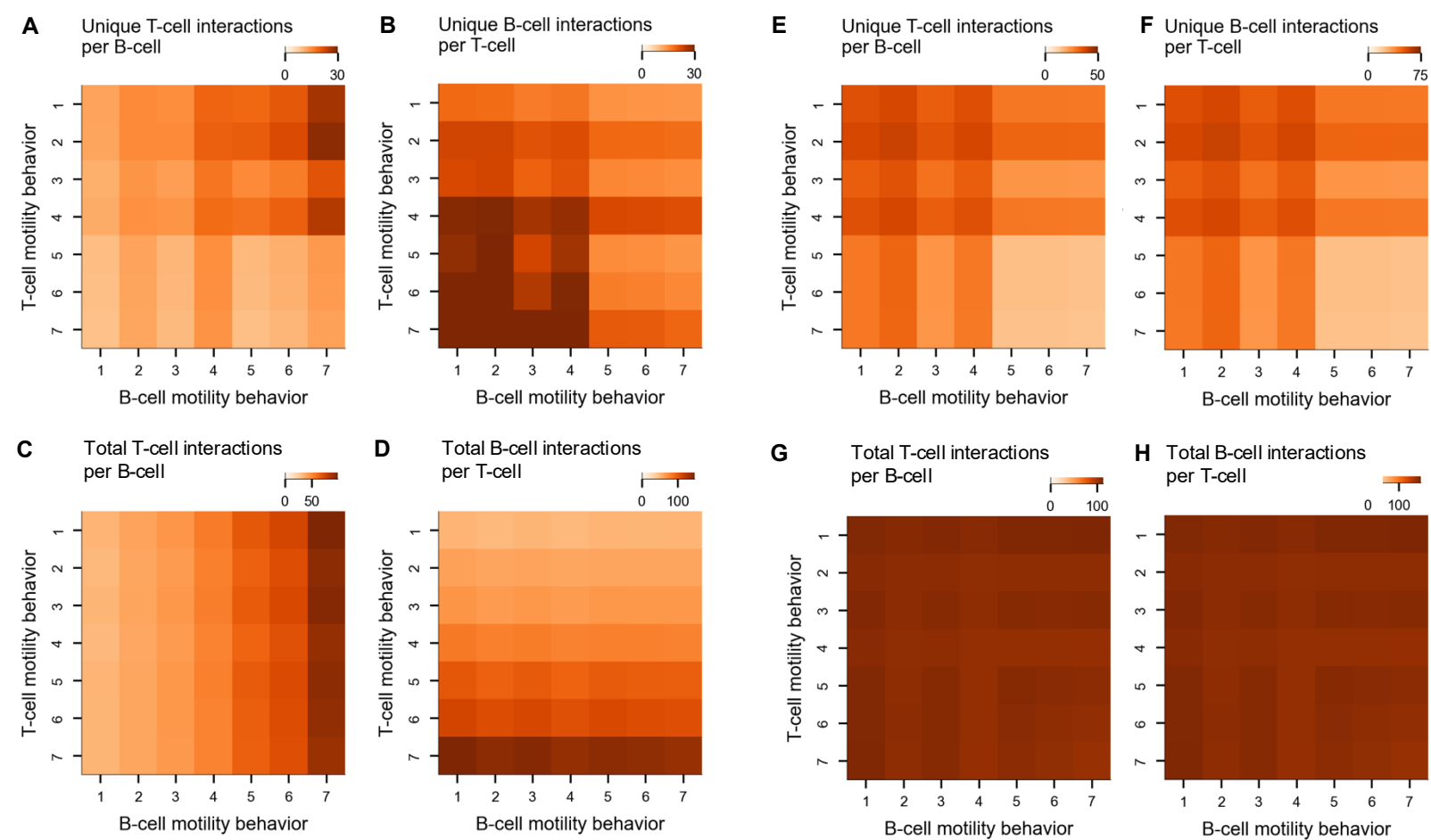


Figure 6. Validation of ABM predictions of GCB-Tfh interactions.



Unique *GCB-Tfh* interactions are maximal within a local environment when *GCBs* move *slowly and tortuously*, while *Tfh*s move *faster and more directly*.

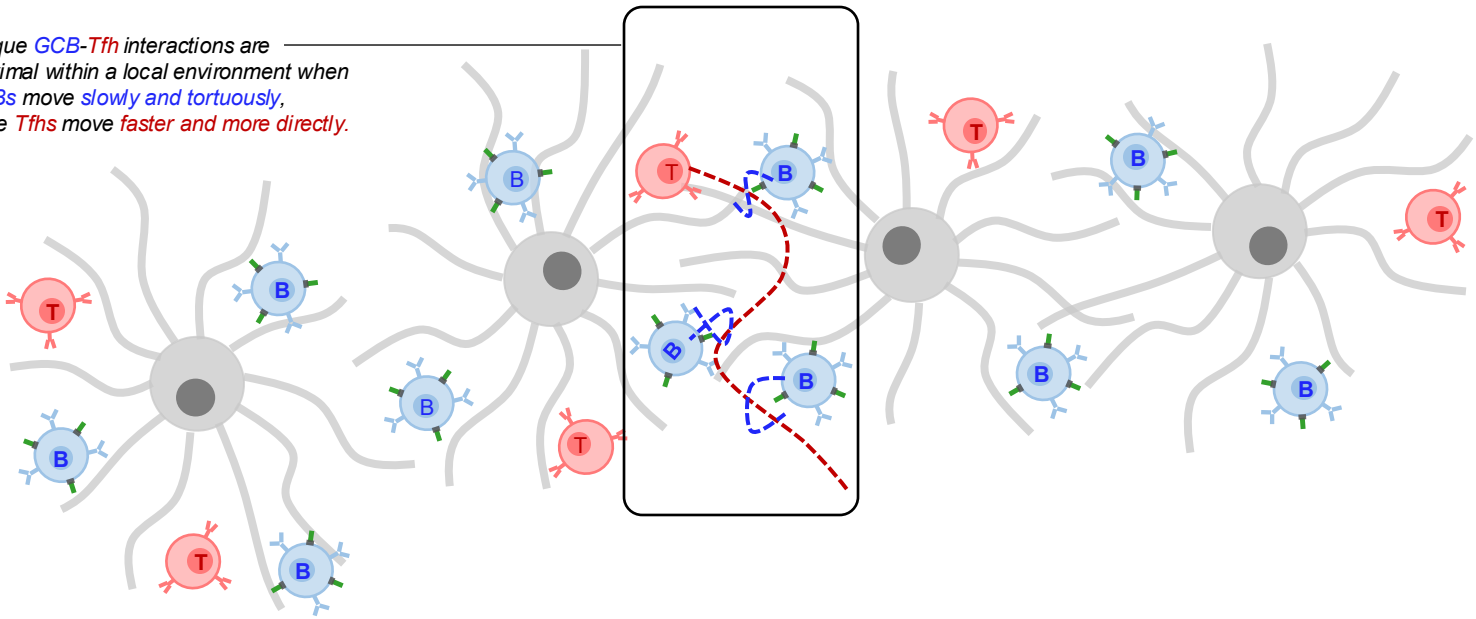


Figure 7. Application of ABM to predict how motility behavior drives unique GCB-Tfh interactions.